UNIVERSITY of CALIFORNIA
SANTA CRUZ

THE DISTRIBUTION OF COALESCING COMPACT BINARIES: IMPLICATIONS FOR GRAVITATIONAL-WAVE OBSERVATIONS

A thesis submitted in partial satisfaction of the
requirements for the degree of

BACHELOR OF SCIENCE

in

ASTROPHYSICS

by

Luke Zoltan Kelley

May 2011

The thesis of Luke Zoltan Kelley is approved by:

Technical Advisor

Professor Enrico Ramirez-Ruiz
Thesis Advisor

Professor David P. Belanger
Chair, Department of Physics

Abstract

The Distribution of Coalescing Compact Binaries:

implications for gravitational-wave observations

by

Luke Zoltan Kelley

Merging compact binaries are the most viable and best studied candidates for gravitational wave (GW) detection by the fully operational network of ground-based observatories. In anticipation of the first detections, the expected distribution of GW sources in the local universe is of considerable interest. Here we investigate the full phase space distribution of coalescing compact binaries at $z = 0$ using dark matter simulations of structure formation. The fact that these binary systems acquire large barycentric velocities at birth ("kicks") results in merger site distributions that are more diffusively distributed with respect to their putative hosts, with mergers occurring out to distances of a few Mpc from the host halo. Redshift estimates based solely on the nearest galaxy in projection can, as a result, be inaccurate. On the other hand, large offsets from the host galaxy could aid the detection of faint optical counterparts. The degree of isotropy in the projected sky distributions of GW sources is found to be augmented with increasing kick velocity and to be severely enhanced if progenitor systems possess large kicks inferred from the known population of pulsars and double compact binaries. Even in the absence of observed electromagnetic counterparts, the differences in sky distributions with varying kick velocity could be readily discernible by GW observatories within the expected accuracies and detection rates of advanced LIGO.

Contents

List of Figures

List of Tables

To my parents;

for their genes,
much of their wisdom,
and all of their love and support.

Acknowledgements

Foremost, I would like to thank my advisor and mentor, Professor Enrico Ramirez-Ruiz.

My appreciation for his unwavering enthusiasm, and tireless dedication to myself and all of his students cannot be overstated. I hope that this body of work will only be the beginning of our collaborations.

I am also grateful to Dr. Adriane Steinacker for the years of support and encouragement. Her passion for aiding in the growth and progress of all those around her has always been an inspiration.

To Dr. Bruce Schumm, I will always be indebted for ushering me into the world of scientific research and investigation. And to Dr. Joshua Deutsch for kindling my passion for science with his always-keen physical insights, in so many lectures and conversations.

Part I

Introduction

Overview

While light is massless, its trajectory is gravitationally altered by massive bodies. In 1915, Einstein showed that gravity can be described as the bending of space-time around objects—which, while cliché, can be thought of as a taught sheet bending under the weight of a bowling ball (for example). Thus, while light would move on a straight path across a smooth sheet, it appears to bend around this distorted version. One of the necessary repercussions of this interpretation, is that massive bodies moving sufficiently violently will cause waves of gravity (or sheet-bends—as per the analogy) to emanate outwards carrying energy with them as "gravitational radiation".

Binary star systems represent the first identified and best understood source of gravitational waves (GW). The stronger the gravity, and the faster the oscillations of the stars, the stronger those waves will be—and thus the more easily they can be detected. Understandably then, the first observation of gravitational waves was via a double pulsar system, in which two neutron stars of masses $1.44M_\odot$[1] and $1.39M_\odot$, orbiting each-other at a distance of less than $3R_\odot$ (Weisberg & Taylor, 2005). These close, dense stars produce gravitational waves which carry enough energy away that the effects on the orbit are measurable as a gradual decay of the orbital period. This *indirect* measurement of GW earned the discoverers—Hulse and Taylor, after which the system is named—the nobel prize in physics, 1993.

Recently, the first gravitational wave observatories (GWOs)[2] have come online, and the first *direct* detection events are expected in the next few years. These instruments, such as Virgo (in

[1] For a list of common units used in the course of this paper, see §A.1.
[2] For a list of common initialisms, see §A.2.

Italy) and the two Laser Interferometer Gravitational-wave Observatories (LIGO, both in America), attempt to measure the oscillation of physical distance as waves pass through the detector. Unique GW signals are expected from stellar pulsations, planetary orbits, and even the big-bang itself; but only the final seconds of double compact object (DCO, or simply, 'compact binary') inspirals are expected to have signals strong enough to observe in the near future. No detections have been made thus far; and LIGO-Virgo are currently undergoing upgrades (to the "advanced" stage) expected to be completed by 2015.

The upgraded detectors will be able to detect GWs with lower amplitude, and thus inspirals at larger distances. The distribution and expected merger rate of DCO systems—composed of two neutron stars (NS-NS; or double neutron stars—DNS), two black-holes (BH-BH; or DBH) or one of each (NS-BH)—have been thoroughly studied over the past three decades, yet uncertainties still span numerous orders of magnitude (e.g., Sadowski et al., 2008; Kim et al., 2005; Fryer et al., 1999; Phinney, 1991; Narayan et al., 1991). None the less, it is clear that these events are exceedingly rare, and thus the event rate is a limiting factor in GW detection. With this in mind, advanced detectors will not only be more likely to detect a GW event at a given distance, they will also probe a significantly larger volume—where there is a much greater chance of an inspiral occurring.

Out of the three types of DCO systems, DNS coalescences are expected to lead the merger rate by at least an order of magnitude, as their constituents are formed from lower mass stars, and thus a far larger population than the high mass stars which form black-holes. NS-NS coalescences are predicted to occur at a rate of $\sim 1^3$ Mpc^{-3}Myr^{-1}, while an optimistic estimate of the distance at which these signals could be detected—the so-called, 'detector horizon'—should be about 400 Mpc for advanced LIGO-Virgo (Abadie et al., 2010). Higher-mass DBH systems, with smaller inspiral separations, could be detected at even larger distances.

The spatial and temporal distribution of mergers is far more complex than the distribution of stars in general. Our understanding of the formation of neutron stars and black-holes alone

[3] 0.01-10 Mpc^{-3}Myr^{-1} at 95% confidence bounds

are imperfect; our knowledge of the pathways by which binary systems form is thus even more tenuous. Still, many of these systems have been observed. Additionally the length of time between binary formation and binary merger (referred to as the system's 'lifetime') can vary significantly, and the overall distribution of lifetimes (i.e. the distribution of initial DCO binary parameters; see §2.1) remains uncertain. Despite the uncertainties, it is known that these systems have large systemic velocities—-up to hundreds of kilometers per second. These velocities have the potential to significantly alter the distribution of these objects in the universe. One of the primary focuses of this study is to explore and quantify the effects of high systemic velocities on the distribution of DCOs.

Single neutron stars are observed to have even larger velocities, up to thousands of kilometers per second. Even slight anisotropies in the formation of NSs can lead to these large "kick-velocities". A one percent anisotropy in a 10^{51} erg supernova, for example, would deliver a kick of about 600 km s^{-1} to a $1.4M_{\odot}$ NS remnant. Fryer et al. (1998) matches the observed proper motions of pulsars, double neutron star systems and x-ray binaries to reach a mean velocity of $\sim 400 - 500$ km s^{-1}. More recently, Hobbs et al. (2005) fits a larger catalogue of pulsar proper motion measurements to a maxwellian distribution with a mean velocity of 400 km s^{-1}. With merger-times after formation frequently on the order of a Hubble time, the distance these objects travel before coalescence can reach megaparsecs. Thus, *a priori*, we would not expect the distribution of merger events (and therein gravitational wave sources) to trace the distribution of stars.

Analyses to date have examined the effects of kick-velocity on the distribution of DCOs using static, model galactic potentials (e.g., Bloom et al., 1999). Zemp et al. (2009) was the first study to employ fully dynamic, cosmologically evolving halo potentials. Here, we expand on those studies to examine in detail the full three dimensional distribution of compact binaries in dynamic environments as a function of natal kick-velocity. In our simulations, we have selected a local-like universe in particular, to investigate the effects of high progenitor speeds on future GW detections. Our results suggest that with a moderate number of detections, the distribution of mergers could

be statistically constrained and thus also the underlying velocity distribution.

In addition to better understanding the physics of compact binaries, the distributions explored here are of great relevance to the GW community. From a theoretical perspective, if the distribution of compact binaries becomes so extended that their merger will occur outside of the light distribution of its host galaxy, and thus there will be a much larger chance of observing an electromagnetic counterpart to the GW signal. Observationally, the expected distribution of these objects must be taken into consideration when these counterparts are searched for. In the moments after a GW detection event, the source location will be poorly constrained. If the DCO distribution is found to trace the distribution of stars, telescopes should be pointed towards the galaxy nearest to the predicted source location. Alternately, if the distribution is extended, telescopes should be pointed to the highest probability location, irrespective of its environment.

The outline of this paper is as follows: in §3.1 we describe the cosmological simulations used and the selection criteria for a local universe analog. In §4 we present the distribution of compact binaries in three kick velocity scenarios, and in §5 we examine detection requirements to distinguish between them experimentally. We show that with sufficient detections and accuracies, the effects of varying kick velocity are readily apparent. Finally, in §6 we discuss our results and their ramifications as–well as mention the prospects of future work. In the appendix are tables of Common Parameters (§A.1), Common Initialisms (§A.2), a section on Orbits (§A.3), and finally a concise, peer-reviewed publication of the work here described (§A.4).

1 Compact Binaries as Gravitational Wave Sources

One of the strongest confirmations of Einstein's theory of General Relativity was the discovery of PSR B1913+16 by Hulse and Taylor in 1974 (Hulse & Taylor, 1974, 1975). This system consists of a pulsar and a companion neutron star, both of mass ~ 1.4 $M_\odot$[1], with an orbital period of $\tau = 0.323$ days (Weisberg & Taylor, 2005). The rapid spatial changes in the mass distributions of tight Double Compact Objects (DCOs) such as these, bend spacetime to such a degree that waves emanate out to infinity. These Gravitational Waves (GW) carry with them a significant amount of energy taken away from the stars' orbital energy, thus decreasing their orbital separation. Figure 1.1 compares the expected and observed period of PSR B1913+16 as a function of time as the orbit tightens.

The formalism of GW emission (derived in §2.1) illustrates that the rate of energy emission is strongly dependent on the orbital separation. If we take Eq. 2.18 (derived in §2.1) as given, we can express the lifetime of the binary system—i.e. the time before merger $\tau_{\rm merge}$—as a function of the initial period τ.

$$\tau_{\rm merge} \approx 5 \times 10^{10} \text{ yr } \left(\frac{\tau}{\rm day}\right)^{\frac{8}{3}} \left(\frac{\mu}{M_\odot}\right)^{-1} \left(\frac{M}{M_\odot}\right)^{-\frac{2}{3}} (1-e^2)^{\frac{7}{2}} \tag{1.1}$$

After inserting an appropriate reduced mass[2] $\mu = 0.7$, and total mass $M = 2.8 M_\odot$, for a double NS

[1] According to Weisberg and Taylor, the masses are so well determined–now after 30 years of observation–that if expressed in grams, the uncertainty would be comparable to that of Newton's gravitational constant itself.

[2] Defined in §A.3

system, we find for the initial orbital period:

$$\tau \approx 0.5 \text{ days } \left(\frac{\tau_{\text{merge}}}{10 \text{ Gyr}}\right)^{\frac{3}{8}} \tag{1.2}$$

Thus, for enough energy to be dissipated such that the stars merge within the age of the universe—that is, a Hubble time ($\tau_h = 13.7$ Gyr)—the initial orbital period must be on the order of a day, corresponding to an orbital separation of $d \approx 4 \times 10^9$ m ≈ 6 R$_\odot$. PSR 1913+16, for example, will merge in $\tau_{\text{merge}} \approx 300$ Myr $\ll \tau_h$.

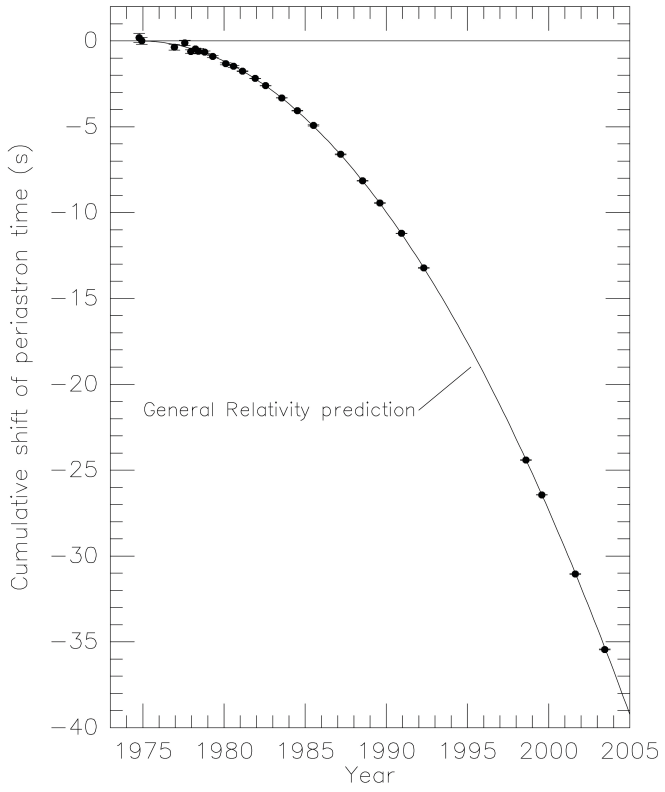

Figure 1.1: PSR 1913+16: Showing the Orbital Decay Due to Gravitational Wave Emission–reproduced from Weisberg & Taylor (2005). The accurate agreement between observations (points) and General Relativistic predictions (solid line) is clearly apparent. Note: the prediction has not been fitted to the data points. This system has an orbital-period decay of $\dot{\text{P}} = -2.42 \times 10^{-12}$ s s^{-1}, and will merge well within a Hubble time.

There are many expected sources of gravitational radiation. Among them are asymmetric stellar oscillations[3] (for a review, see: Andersson, 2003) and rotations (e.g. Horowitz, 2010), supernovae (e.g. Fryer et al., 2004; Ott et al., 2004), cosmic strings (e.g. Damour & Vilenkin, 2001; Ölmez et al., 2010), and even inflation and phase-changes associated with the big bang (e.g. Smith et al., 2006; Grojean & Servant, 2007). The final merger of two, solar-mass, neutron stars (NSs) or black-holes (BHs), referred to here as double compact objects, are believed to be the best candidates for the first, and the majority of, detectable signals for many reasons. The first gravitational wave detections are expected to be at very low signal-to-noise ratios, and thus highly periodic signals can be more easily deconvolved from background noise than transient events like supernovae. At the same time, periodic sources like stellar oscillations, planetary systems, or binaries of main-sequence stars (or even white-dwarfs) would produce much lower magnitude GW signals due to their weaker, and more diffuse gravitational fields, and slower rates of oscillation. Finally, binaries of super-massive black-holes at the center of merging galaxies may meet the aforementioned criteria, but their inspiral signals will be of lower frequency than that of LIGO-Virgo's sensitivity band (see Fig. 2.3).

It has long been known that a large portion of stars exist in binary systems[4], however much less is known about DCOs as only a hand-full of such objects (all DNS systems) have been observed (see Table 1.1). More than half of these objects have sufficiently close orbits (i.e. periods $\tau < 0.5$ days) to merge within a Hubble time—often referred to as 'coalescing' compact binaries. The orbital separation of such systems is significantly smaller than the radii of their progenitors; begging the question of how they were able to form, evolve and survive into such exotic configurations.

1.1 Formation Pathways

Stars with initial masses greater than $\sim 10 M_\odot$ proceed through thermonuclear evolution until iron-peak metals with optimally stable nuclei are produced, at which time they are prone

[3] While strong enough signals from our own sun are unlikely, they are not excluded by current observations (e.g. Cutler & Lindblom, 1996).

[4] A classic paper by Duquennoy & Mayor (1991) argues for a binary fraction near 2/3 for massive main-sequence stars, while more recent studies including lower mass stars suggest the fraction could be more like 1/3 (Lada, 2006).

DNS Name	Distance (pc)	Period (days)	Reference
PSR J1518+4904	700	8.63	Nice et al. (1996)
PSR J1811-1736	6000	18.78	Lyne et al. (2000)
PSR J1829+2456	1200	1.18	Champion et al. (2004)
PSR B1913+16	1200[1]	0.323	Hulse & Taylor (1975)
PSR B1534+12	500	0.421	Wolszczan (1991)
PSR J1756-2251	2500	0.320	Faulkner et al. (2005)
PSR J0737-3039	500	0.1	McLaughlin (2003)
PSR B2127+11C	9700	0.335[2]	Wolszczan et al. (1989)
PSR J1906+0746[3]	5400	0.166	Lorimer et al. (2006)

Table 1.1: List of Known Double Neutron Star (DNS) Systems. Binaries with orbital periods of less than half a day will merge within a Hubble time, due to the emission of gravitational radiation. During the final seconds of coalescence, gravitational wave emission is expected to be at detectable levels.

to instabilities leading to gravitational collapse via supernova (SN) explosion (Heger et al., 2003; Postnov & Yungelson, 2006). The resulting neutron stars are prevented from further collapse by neutron degeneracy pressure. If, however, the initial mass of the star exceeds $\sim 25 - 30\ M_{\odot}$, degeneracy pressure is insufficient to prevent its complete collapse into a black-hole[5].

Binaries with two of these highly compact remnants can form via numerous pathways—the most significant of which are outlined below in Table 1.2, and described in detail by Fryer et al. (1999). In each case, two supernovae must occur; and further, to achieve the observed small orbital separations, the systems must generally pass through a common envelope (CE; see §1.2 and references therein) phase in which one star is engulfed by the expanding envelope of the other. Viscous forces and dynamical friction dissipate orbital energy, and with it the orbital separation (e.g. Portegies Zwart & Yungelson, 1998; Fryer et al., 1999).

[5]For a more comprehensive review of the outcomes of massive-star evolution, see Heger et al. (2003).

Type	#	Description
DNS	1	Primary of massive binary evolves off the main-sequence, overfills its Roche-lobe and transfers mass to the secondary. The primary explodes leaving a NS remnant. As the secondary evolves, its envelope engulfs the primary—the two undergo CE evolution. The orbit tightens, and the CE is ejected leaving a NS He-star binary. He-star supernovas resulting in a DNS system.
	2	Initially like '1' above, except the CE phase precedes both supernovae. Two He-stars share an envelope, tightening the orbit. The CE is ejected leaving a double He-star binary. Two consecutive SNe yield a DNS system.
BH-NS	3	Initially as in '1', the primary star transfers mass to the secondary until it explodes, in this case collapsing into a BH. The BH enters a CE with the secondary, after CE ejection a second SN produces a NS and a tight BH-NS system.
	4	Initially as '1', except the accreting NS—while in the CE—collapses into a BH, with the explosion ejecting the envelope. The He-star evolves into a NS, resulting in a BH-NS binary.
DBH	5	The same as '3' except the second SN results in a BH, leaving a BH pair.
	6	The same as '4' except the second SN results in a BH, leaving a BH pair.
	7	Nonconservative mass transfer between two initially very massive stars tightens the orbit, followed by two consecutive supernovae, each yielding a BH remnant.
	8	Dynamic formation In the dense cores of globular clusters (GC), either via tidal capture or three-body interactions. While dynamic formation of DNS systems is certainly possible, it is not expected to contribute as significantly to the overall population.

Table 1.2: Double Compact Object Formation Pathways. In each of the above pathways (except #8), a binary system of two massive stars with orbital separations less than a few AU evolves into a binary with orbital separation $d \lesssim 0.5\ R_\odot$, composed of two compact objects—double neutron stars (DNS), double black-holes (DBH), or one of each (BH-NS).

The typical formation pathway is outlined as #1 in Table 1.2, and illustrated in Fig. 1.2. Starting with a binary of two massive stars with an initial orbital separations on the order of an astronomical unit (AU), the primary (more massive star) evolves off of the main sequence and overfills its Roche-lobe—transferring mass to the secondary. Typically (as in routes: 1,3-6), the primary then explodes leaving a remnant NS (1, 4) or BH (3,5-6). As the secondary evolves, its expanding hydrogen envelope encompasses the compact primary in a common envelope (discussed further in §1.2). In route #2, the CE phase precedes the first supernova and contains two He-cores instead of a He-core and remnant. It is possible that a NS, rapidly accreting in a common envelope, would exceed the Tolman-Oppenheimer-Volkoff limit (Tolman, 1939; Oppenheimer & Volkoff, 1939) and collapse into a BH (4,6). During the CE phase which tightens the orbit by about two orders of magnitude, the envelope is ejected, leaving a tight He-star–BH/NS binary. A second supernova (or both supernovae in path #2) occurs in which the He-star collapses into a NS (1-4) or BH (5,6). Thus, pathways 1-6 proceed through a common envelope to yield a tight double compact object.

Results by Belczynski et al. (2007) suggest that formation of DBH systems through CE could be rare, as they may tend to merge completely. If this is the case, an

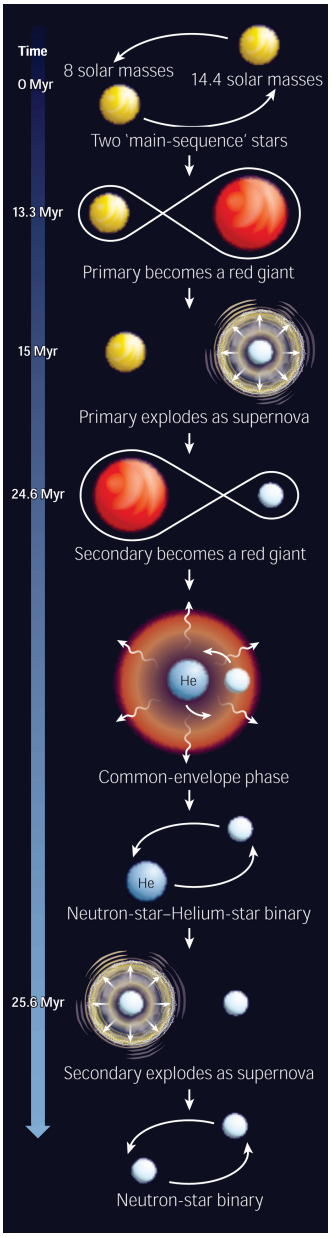

Figure 1.2: Characteristic Double Compact Object (DCO) Formation Pathway via Common Envelope (CE) Evolution–modified from Ramirez-Ruiz & Lee (2009). Starting with a massive binary star system, the common envelope decreases the orbital separation and two supernovae yield a coalescing compact binary.

alternate formation scenario (route #7) may dominate their formation. In this case, non-conservative mass transfer between two very massive stars tightens the orbit sufficiently (e.g. Belczynski et al., 2007), and two SNe each yield a black-hole. This pathway would be negligible if the stars survived common envelope evolution.

Finally, dynamic formation is possible in the dense cores of globular clusters in which stellar encounters are more common. Especially in the case of NS–giant close encounters, a subsequent CE phase could be likely for newly bound systems (e.g. Davies et al., 1992). Tidal capture and three body interactions (e.g. Lee et al., 2010; Banerjee et al., 2010) would favor the highest mass stars and thus DBH systems. Data from the distribution of Low-Mass X-ray Binaries and High-Mass X-ray Binaries suggest that while dynamic formation of tight binaries does occur, its contribution to the overall population may be small (see Iben & Livio, 1993).

1.2 Common Envelope Evolution

Double compact binaries hold dichotomous traits: they are of interest due to their incredibly close orbits; yet, individually, their progenitors must necessarily have been orders of magnitude larger in size. The resolution to this evolutionary puzzle was first suggested by Paczynski (1976), in the context of Cataclysmic Variable formation, and Ostriker (1975), for NS-containing binaries. These authors were aware that contact binary systems (e.g. W Ursae Majoris binaries), are a further entangled version of the established mass transferring systems, like cataclysmic variables and high-mass X-ray binaries. They reasoned that systems could be formed by stars coupled further still—such that one star is entirely engulfed by the envelope of the other. These common envelope situations are fundamentally unstable with lifetimes less than thousands of years, thus differing from dynamically stable contact binaries with lifetimes of millions or more years. In this section we review the basic features of CE evolution as it pertains to double compact objects. For a more comprehensive review, see Taam & Sandquist (2000) and Taam & Ricker (2010).

The high mass stars ($\gtrsim 5$ $M_\odot$) which form NSs and BHs will naturally evolve off of the

main sequence (MS) upon cessation of hydrogen burning, expanding into (super)giants over a thermal (Kelvin-Helmholtz) timescale. These giants reach radii of up to tens of AU (hundreds of $R_\odot$), thus any massive binary with an initial period of less than about 10 yrs can enter a CE phase. Onset of tidal evolution is further aided by tidal effects between the primary's envelope and the secondary, which will tend to spin-up the giant envelope at the expense of orbital angular momentum. Especially for higher mass ratios and initially smaller orbital separations, tidal instabilities alone will pull the secondary into the primary's envelope (Counselman, 1973; Meyer & Meyer-Hofmeister, 1979). Once the giant's surface exceeds the inner Lagrangian point, and thus the Roche lobe, mass transfer begins. For smaller mass ratios, and in general whenever the thermal timescale of the accretor is significantly longer than the mass-transfer timescale (Iben & Livio, 1993), the secondary will be unable to accrete the mass being transferred, and a common envelope will form around the system (Taam & Sandquist, 2000).

After the secondary fully enters the CE, rapid in-spiral begins. The orbital velocity is generally supersonic and thus a conical shock forms around the secondary. Accretion is hydrodynamically limited, and significant drag results from the bow-shock and gravitational wake (Bondi & Hoyle, 1944). Additionally, once the stellar cores near, spiral-shocks extend throughout the envelope better facilitating transfer of angular momentum from the orbit to spin of the common envelope. Fig. 1.3 shows density contours in the orbital and perpendicular planes of CE evolution at numerous times. The spiral shock structure can be seen between 2610 and 3814 days in the orbital plane. The CE phase is also very effective at transferring energy from the orbit into the envelope, decreasing its binding energy, and inflating the envelope—as seen along the perpendicular plane. Overall the CE phase lasts $\lesssim 1000$ yrs, and decreases the orbital separation by a factor ~ 100 (e.g. Terman et al., 1995). The evolution of the orbital separation in a characteristic situaton is illustrated in Fig. 1.4. In general, systems with more evolved giants experience more rapid in-spirals, as a larger fraction of their mass is in the outer layers of the envelope.

In the case of a NS in a common envelope with a (near) main-sequence star, the binding

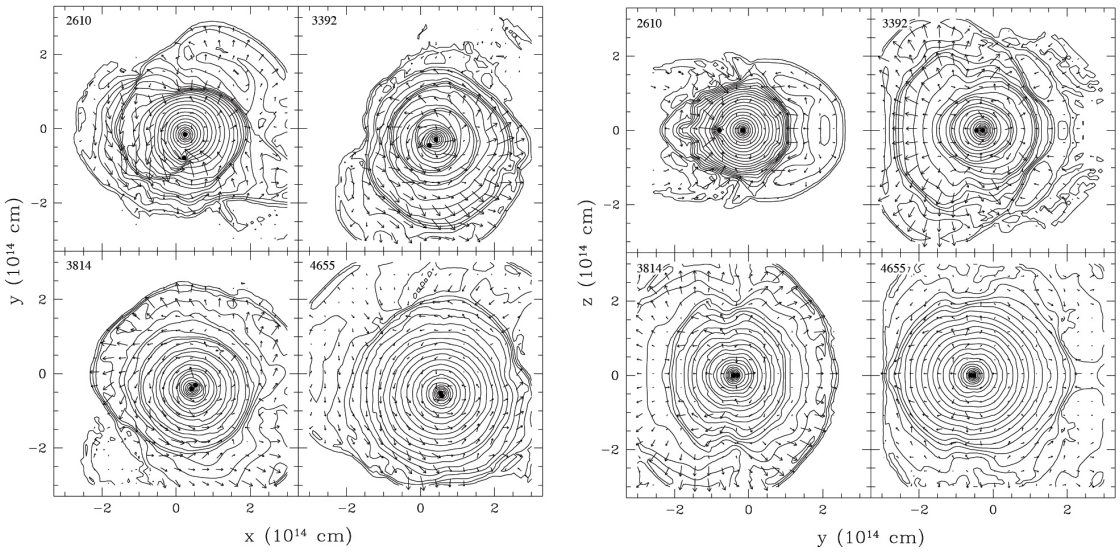

Figure 1.3: Hydrodynamic Simulations of Common Envelope Evolution—Reproduced from Taam & Sandquist (2000). Hydrodynamic simulations of a 1.4 $M_\odot$ neutron star in a CE with a 20 $M_\odot$ red supergiant are illustrated with density contours along the orbital (left panels) and perpendicular (right panels) planes. Snapshots are labeled by days after onset, at 2610, 3392, 3814, and 4655 days. The spiral shock structure, and orbital separation decrease are clearly apparent.

energy of the envelope would be too great to be ejected by the orbital energy. In this situation, in-spiral would most likely continue to coalescence. This may also be the case for less evolved (yellow/blue) and lower-mass (red) giants, as the envelopes mass is too centrally condensed; and additionally for initially short-period systems ($\lesssim$ 100 days) like some high-mass X-Ray binaries (Taam & Sandquist, 2000). In the case of core-merger, the formation of a Thorne-Zytkow object is possible—resembling a red supergiant with a neutron-degenerate core (Thorne & Zytkow, 1975, 1977; Taam & Sandquist, 2000). Stability of such a system would require Eddington-limited accretion to avoid the neutron star's collapse into a black-hole, disrupting the envelope. Chevalier (1993) and Brown (1995) suggest that NS accretion, even in the CE phase, may not be limited to the Eddington rate as accretion flow temperatures could be sufficient for neutrino dominated cooling, leading to significantly super-Eddington accretion (e.g. Zel'Dovich et al., 1972)—and thus potential collapse to a BH. This may be avoided however if the angular momentum of the inflowing material limits accretion (Chevalier, 1996).

Once the NS reaches the high-density region near the giant's core (i.e. within a few solar

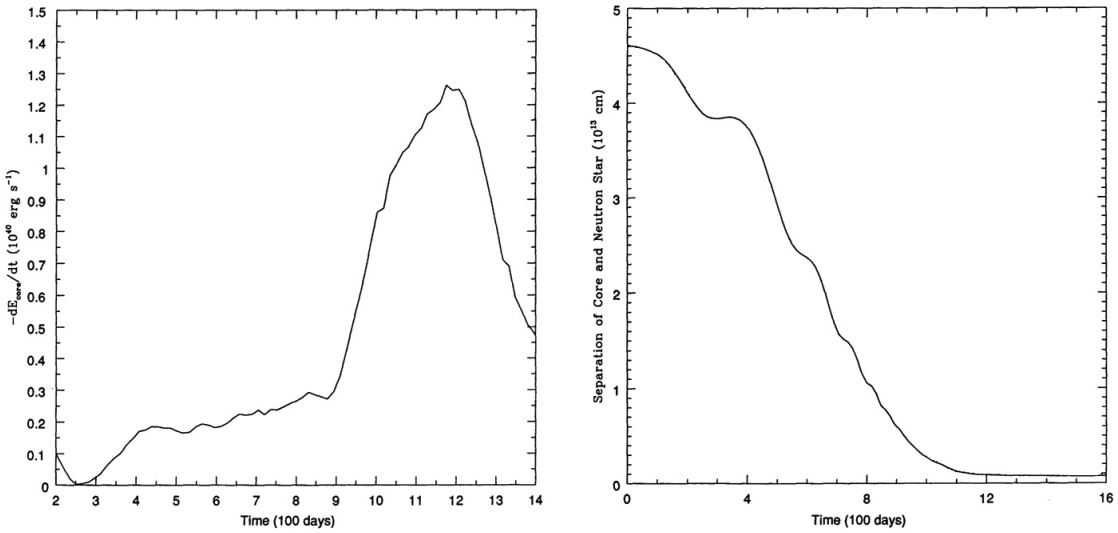

Figure 1.4: Evolution of Energy Deposition into the Envelope (left panel) and Orbital Separation (right panel) During Common Envelope Phase—Reproduced from Terman et al. (1995). These results, from the CE of a NS and red supergiant, illustrate the rapid decrease of orbital separation on timescales $\sim$ 1000 yrs. Once the NS and supergiant-core are within a few solar radii, the local material is cleared out—slowing the rate of inspiral. At the same time ($\sim$ 900 days), rapid energy deposition into the now corotating local envelope accelerates the rate at which material is ejected from the system.

radii), the major phase of mass loss begins. Once the cores are this close, a local region of the envelope within a few orbital separations is spun-up to co-rotation, while the outer layers of the binary remain asynchronous increasing energy deposition and mass-loss. This is apparent near 900 days in Fig. 1.4, where the change in orbital separation levels off, and energy deposition into the CE rises dramatically. The energy input from the cores can reach $\sim 10^{40}$ ergs s^{-1} producing mass loss rates of $\sim 1 M_\odot$ yr^{-1} (Taam & Sandquist, 2000). The efficiency with which orbital energy ejects the envelope is measured by a parameter α_{CE}, such that

$$\alpha_{CE} \equiv \frac{E_{\rm bind}}{\Delta E_{\rm orb}} \approx \frac{a_f}{a_f^0} \tag{1.3}$$

where $E_{\rm bind}$ is the binding energy of the envelope, $E_{\rm orb}$ is the change in energy of the orbit; and a_f and a_f^0 are the actual and ideal (100% efficiency) final separations respectively (e.g. Livio & Soker, 1988). Thus α_{CE} describes how effectively the orbit is tightened, and must be sufficiently large to prevent in-spiral, but small enough to explain the observed separations of DCO systems. General expectations are $\alpha_{CE} \approx 10 - 50\%$ (Livio & Soker, 1988; Terman et al., 1995; Taam & Sandquist,

2000; Taam & Ricker, 2010; Zorotovic et al., 2010), depending on the masses and evolutionary states of the stars.

In general, efficient energy transport leads to decreases in the CE ejection efficiency as energy transported to the surface is radiated away. Other sources of energy deposition could play a roll in bolstering α_{CE}. For example, enhanced nuclear shell burning or recombination energy in the ionization zones of the envelope (see: Iben & Livio, 1993). Nuclear energy may be insignificant over the short time scales of mass-ejection however, and recombination would most likely only assist in the ejection of the outer most layers of the envelope—instead of towards the center where most of the mass resides, and the most energy is required (see Sandquist et al., 2000). There is some evidence to support occasionally high values of α_{CE}, possibly even greater than unity (Kalogera, 1999).

1.3 Supernova Kicks

Two supernovae are required to yield each double compact object, regardless of the specific formation pathway. Each of these supernovae typically releases between 10^{49} – 10^{50} ergs of energy. Even slight anisotropies in these explosions can bestow huge recoil velocities to the resulting stellar remnant. It comes as no surprise then, that significant evidence exists for the presence of large (in some cases ≥ 1000 km s^{-1}) velocities in the neutron-star population. The existence of these 'Natal Kicks' has been established by NS–supernova remnant associations (e.g. Camilo et al., 2009), proper motion surveys (e.g. Lyne et al., 1982), and the orbital parameters of X-Ray binaries (e.g. Fryer et al., 1998).

Consider the guitar nebula (B2224+65, Cordes et al., 1993), depicted in Fig. 1.5. The velocity of this NS can be constrained by association with the nebula, the angle of the bow-shock, and even the change in position over years of observation. These measurements constrain the pulsar's velocity to $\gtrsim 800$ km s^{-1}. The strongest body of evidence, however, comes from evolutionary studies of DCOs. Hansen & Phinney (1997) compared the (then known) sample of pulsar proper motions

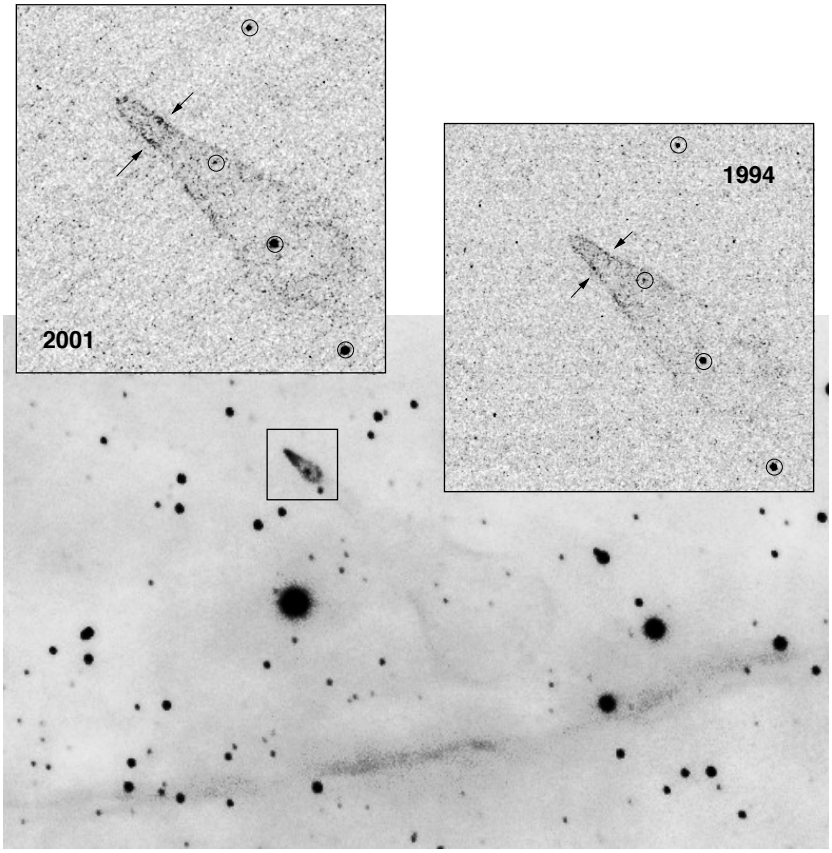

Figure 1.5: Hα images of the Guitar Nebula–reproduced from Chatterjee & Cordes (2004). The NS is located at the very tip of the shock in each image. This wide-field image was obtained from the 5m Hale Telescope at Palomar, while the high-resolution insets of the boxed region were taken with HST in 1994 (right) and 2001(left). This radio pulsar is traveling at $\sim 800 - 1600$ km s^{-1}.

to simulations; their best fit distribution was Maxwellian, with a mean of $\sim 250 - 300$ km s^{-1}, and dispersion $\sigma_v = 190$ km s^{-1}. Fryer et al. (1998) performed a similar analysis, with the addition of X-ray binaries and DNS systems to the sample space; they found a mean velocity of ~ 500 km s^{-1}, but noted that a bimodal distribution was more consistent, with peaks at 0 km s^{-1} and 600 km s^{-1}. The authors note, however, that the bimodal distribution might be an anomaly from inaccurate distance measurements[6]. More recently, Hobbs et al. (2005) studied a sample of 73 younger pulsars (ages less than 3 Myrs), and found a mean velocity of 400 km s^{-1}, and overall Maxwellian distribution with standard deviation $\sigma_v = 265$ km s^{-1}. The results from these classical studies are presented in

[6]This is consistent with the results and distance measurements of Hobbs et al. (2005). At the same time, however, Arzoumanian et al. (2002) find a similar bimodal distributions.

Table 1.3.

Although the existence of such large natal kicks is observationally known, the specific mechanisms for producing them remain uncertain. The fundamental issue is how to produce the required asymmetries—on the order of a few percent. Possible mechanisms can be grouped into three classes: hydrodynamic, neutrino, and exotic. For the first two classes, we follow the discussion of Lai (2000) and references therein.

Reference	Mean Velocity (km s^{-1})	Variance (km s^{-1})	Type
Hansen & Phinney (1997)	250	190	Maxwellian
Fryer et al. (1998)	500	-	Bimodal
Hobbs et al. (2005)	400	265	Maxwellian

Table 1.3: Estimates for mean natal kicks based on observations and simulations. Although the mechanisms to deliver such kicks remain largely uncertain, objects are known to have kicks in the range of 100 – >1000 km s^{-1}.

Hydrodynamic mechanisms require initial asymmetries in the pre-collapse stellar core, which lead to asymmetries in matter ejection (and to a lesser extent neutrino emission). Core asymmetries are believed to arise from pre-supernova perturbations, and become enhanced during the explosion. Oscillatory gravity-modes (g-modes) are constrained to the core due to stratified convection zones, and driven by the ϵ-mechanism in which a small density perturbation on one side of the star gives way to increased nuclear burning. Enhanced burning then increases the local pressure, which propagates through the star and causes another density perturbation on the opposite side.

Neutrino driven asymmetries rely on a far more subtle mechanism—the parity violation induced by strong magnetic fields. The cross section of neutrino-producing ('Urca') processes depend on the relative orientation of the magnetic field and neutrino momentum[7](e.g. Arras & Lai, 1999). Additionally there could be a net drift flux along the magnetic field due to ν_e and $\bar{\nu_e}$. Under the category of exotic mechanisms, additions to the standard model have been proposed—e.g. a

[7]This direction dependence may, however, be smoothed out by scattering (Lai, 2000).

'sterile neutrino'–which follows the same formation processes but has a much lower cross-section of interaction with nuclear matter (e.g. Kusenko, 2005).

The first order effects of supernova explosion on binary dynamics can be examined analytically, regardless of the kick mechanism. Consider a supernova in which the primary star loses some fraction of its mass $1-\epsilon$, resulting in $M_1' = \epsilon M_1$; and receives a kick of magnitude w, resulting in a relative velocity:

$$\vec{V}_f = \vec{V}_i + \vec{w} \tag{1.4}$$

where the subscript 'i' and 'f' refer to initial and final respectively. The system[8] remains bound if

$$\mu_f \frac{V_f^2}{2} - \frac{GM_1M_2}{a_i} < 0 \quad \rightarrow \quad \frac{V_f^2}{V_i^2} < 2\frac{M_f}{M_i} \tag{1.5}$$

If there were no kick-velocity (i.e. $\vec{V}_f = \vec{V}_i$), the binary would become unbound if more than half of the total mass was lost in the explosion. A kick which decreases the net velocity allows more mass to be lost, and *visa versa*. In some DCO formation scenarios—namely, a stellar-mass neutron star along with a giant who's core mass $M_{core} \gtrsim 4.2M_\odot$—an auspicious kick would be required to keep the system bound (Taam & Sandquist, 2000).

The problem is further complicated by two sequential kicks, preceding and or intervening common envelope phases, and significant mass-loss via winds, Roche-lobe overflow, and common envelope ejection. Based on observations, however, the resulting barycentric velocities can be constrained. Fryer & Kalogera (1997), for example, find a minimum center-of-mass (COM) velocity of ~ 200 km s^{-1} for the short-period DNS systems PSR 1913+16 and PSR 1534+12 (see table 1.1), consistent with other studies (e.g. Thorsett et al., 2005). Population synthesis simulations find similar results, with mean COM velocities of $\sim 200 - 300$ km s^{-1} (Belczynski et al., 2002; Portegies Zwart & Yungelson, 1998; Fryer et al., 1999). Figure 1.6 shows characteristic COM velocities after the second SN in DNS, DBH, and BH-NS systems respectively, from Belczynski et al. (2002).

[8]For a brief review of the relevant orbital parameters, see § A.3.

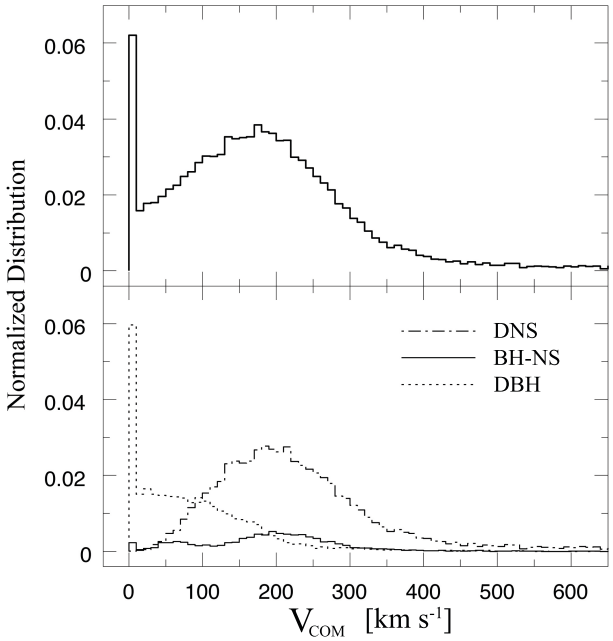

Figure 1.6: Center of Mass Velocities for DCOs, Post Second Supernova–reproduced from Belczynski et al. (2002). The cumulative distribution (top panel) shows the net result of all DCO subtypes (bottom panel). The large peak at zero velocity is due to DBH systems in which both black-holes were formed by direct-collapse–assumed to be isotropic.

1.4 The Double Compact Object Population

In anticipation of direct gravitational wave detections, the last two decades have seen extensive research on the expected rates of gravitational wave signals. DCO in-spirals are not only the best understood candidates for GW signals, but the only type expected to be detectable by Virgo-LIGO. Here we describe the expected detection/merger rates, and the existing research on the distribution of in-spiral progenitors. In §2.2 we describe the basic operational principles of current GW observatories.

In a classic paper, Narayan et al. (1991), examines the 3 DCO systems[9] known—while taking into consideration the fraction of the sky which had been surveyed—at the time, to reach an expected merger rate of ~ 1 yr^{-1} within 200 Mpc h^{-1} for DNS systems (and a comparable rate for BH-NS systems). In another classic paper, Phinney (1991) used B-band luminosity–as a tracer of the star formation rate–combined with the observed binary fraction, to estimate an expected DNS

[9]DNS systems PSR 1534+12, PSR 1913+16 and also what is now believed to be a NS-WD system PSR 2303+46.

merger rate of ~ 1 yr^{-1} within 200 Mpc h^{-1}, and roughly the same for DBH and BH-NS systems.

More recently, studies such as Kalogera et al. (2004) have continued these types of calculations with more rigorous statistics and new observations to refine the estimates. The same group has also employed the same precision in population synthesis models to explore the subject, and especially DBH and BH-NS systems, from an alternate direction (Kalogera et al., 2007; O'Shaughnessy et al., 2008). These, most recent, results are a factor of ~ 100 lower than those of 1991. Table 1.4 summarizes these findings as seen in Abadie et al. (2010).

Source	R_{low} (Mpc^{-3} Myr^{-1})	R_{mean} (Mpc^{-3} Myr^{-1})	R_{high} (Mpc^{-3} Myr^{-1})	Reference
DNS	0.01	1	10	[1]
BH-NS	6×10^{-4}	0.03	1	[2]
DBH	1×10^{-4}	5×10^{-3}	0.3	[3]

Table 1.4: Expected merger rates of DCOs per Mpc^3 per Myr. Internal references: [1] - Kalogera et al. (2004); [2] - O'Shaughnessy et al. (2008); [3] - Kalogera et al. (2007). R_{low} and R_{high} are 95% confidence intervals around the probability density function mean R_{mean}.

Merger times are generally found to be relatively insensitive to kick-velocity (Bloom et al., 1999; Fryer et al., 1999, O'Shaughnessy, R., private communication, 2010), however, a study by Portegies Zwart & Yungelson (1998) suggests that high velocity systems tend to merge in shorter time scales. Estimates of DCO mean merger times range significantly, but most estimates lie between 10^8 yrs (e.g. Bloom et al., 1999) and 10^9 yrs (e.g. Portegies Zwart & Yungelson, 1998). Such long lifetimes, combined with large velocities, allow these objects to travel up to megaparsecs before they merge, possibly leading to large discrepancies between their distribution and that of baryonic matter (stars and gas).

Ours is the first study to perform a detailed examination of the full phase-space distribution of DCOs in fully dynamic simulations of a local like universe. More limited studies have been performed in the past, however. Figure 1.7–reproduced from Bulik et al. (1999)–shows the cumulative distribution of DCOs in a MW-like potential for numerous kicks; these results are characteristic of

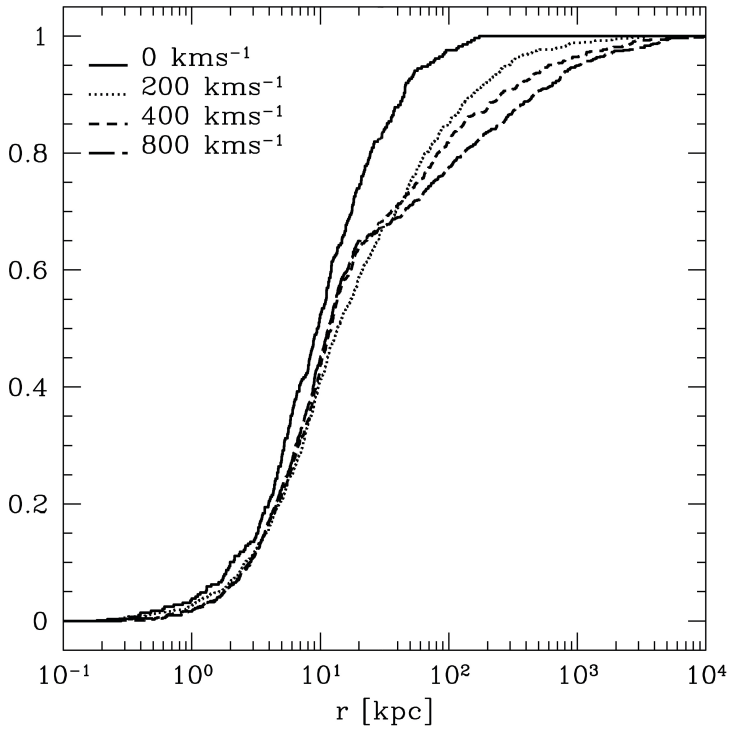

Figure 1.7: Cumulative distribution of DCO vs. Projected Distance from a Milky-Way like Galaxy for Numerous Kick Velocity Models–reproduced from Bulik et al. (1999). These results are characteristic of early studies of compact binary distributions, evolving in static potentials of an isolated galaxy.

this type of study (see also: Portegies Zwart & Yungelson, 1998; Fryer et al., 1999). Work by Zemp et al. (2009), which we continue, has shown that DCO retention is actually much lower, when the environment and dynamic history of the host halos are considered.

2 Gravitational Radiation and Observation

Radiation is any mechanism by which energy can be transported from a source to arbitrarily large distances. The standard example is light (electromagnetic radiation), but the existence of non-photonic radiation has been known since the work of Becquerel, and the Curies at the end of the 19^{th} century. Radiation not only caries energy out to infinity, but also information–such as that recovered by optics-based telescopes since Galileo. More recently, non-photonic radiation has been used to the same end. Super-Kamiokande, for example, was the first experiment to confirm neutrino flavor oscillations (e.g. Fukuda et al., 1998); and HiRes has been delivering high-resolution maps of the high-energy cosmic ray sky for many years (e.g. High-Resolution Fly's Eye Collaboration et al., 2007).

In the last decade, construction has been completed on the first-ever gravitational wave observatories (GWO) marking the first example of not only non-photonic but also non-particulate astronomy. The Laser Interferometer Gravitational-Wave Observatory (LIGO), for example, is a joint project headed by Caltech and MIT (also involving numerous other institutions) which began operation in 2002, and reached design efficiency in 2005 (Abbott et al., 2009). Similar projects exist across the globe with Tama in Japan (Takahashi & the TAMA Collaboration, 2004); the German-UK GEO, based in Germany (Lück et al., 2006); and Virgo in Italy by the European Gravitational Observatory (Acernese et al., 2006). While no GW detections have been made to

date, even pessimistic estimates for event-rates and detector sensitivities suggest that detections are extremely likely in the next decade—especially following the current upgrades to the LIGO detectors.

The detection of gravitational wave signals is the ultimate motivation of the present study. The physics of gravitational waves and the remarkable engineering required to detect them is becoming an expansive and intricate field in-and-of themselves. In §2.1, we present a basic motivation for the existence of gravitational waves and some of their key features. A discussion of GW detectors follows in section §2.2.

2.1 Gravitational Waves

For a rigorous analysis, see Landau & Lifshitz (1975), Hartle (2003), or Hughes (2009); alternately, for a concise, yet detailed overview see Peters (1964). Einstein's field equations, in the standard formalism[1]:

$$R_{\mu\nu} - \frac{1}{2} g_{\mu\nu} R = -8\pi G T_{\mu\nu} \tag{2.1}$$

relates the effects of mass & energy (the stress tensor $T_{\mu\nu}$–right hand side) to the geometry of spacetime (the metric tensor $g_{\mu\nu}$–left hand side)[2]. We can linearize the field equations by assuming weak perturbations[3] to the galilean metric (flat spacetime):

$$g'_{\mu\nu} = g_{\mu\nu} + h'_{\mu\nu} \tag{2.2}$$

Linearization introduces some gauge arbitrariness, resolved by introducing appropriately chosen supplementary conditions, namely $h_{\mu\nu} = h'_{\mu\nu} - \frac{1}{2}\delta_{\mu\nu} h_{\lambda\lambda}$. We can then rewrite Eq. 2.1 as

$$\Box h_{\mu\nu} = \left(\frac{1}{c^2} \frac{\partial^2}{\partial t^2} - \nabla^2 \right) h_{\mu\nu} = -16\pi T_{\mu\nu} \tag{2.3}$$

where $\Box \equiv \frac{\partial^2}{\partial x_\mu \partial y_\mu}$ is the d'Alembertian operator.

[1] We use Einstein's summation notation $a_\mu b_\mu = a_1 b_1 - (a_2 b_2 + a_3 b_3 + a_4 b_4)$.

[2] The Ricci curvature tensor ($R_{\mu\nu}$ and there-in the Ricci scalar curvature, is a function of the metric tensor and its derivatives.

[3] Self-consistent with the resulting perturbation amplitudes (e.g. Eq. 2.15).

If we consider a region of empty space we see that this simplifies to the classical wave equation (i.e. $\Box h_{\mu\nu} = 0$). If we examine a plane-gravitational wave

$$\left(\frac{\partial^2}{\partial x^2} - \frac{1}{c^2}\frac{\partial^2}{\partial t^2}\right) h_\mu^\nu = 0 \tag{2.4}$$

we find solutions as a function of $t \pm \frac{x}{c}$, corresponding to waves traveling in the negative and positive x-direction. Such plane waves (described by an energy density $h_{\mu\nu} = he_{\mu\nu}\cos[\omega t - \vec{k}\cdot\vec{x}]$) can be characterized by a polarization tensor ($e_{\mu\nu}$). After choosing a suitable gauge, we arrive upon a pair of polarizations separated by an angle of $\frac{\pi}{4}$, generally designated h_+ and $h_\times$. By analogy to electromagnetism, we can immediately conclude that the energy-momentum (pseudo-)tensor will be proportional to the product of two components of the perturbation tensor ($h_{\mu\nu}$), for each independent polarization[4], i.e.

$$t^{\mu\nu} \propto h_+^2 + h_\times^2 \tag{2.5}$$

The full solution to the linearized Einstein equations (Eq. 2.3) with the presence of source terms is (Peters, 1964)

$$h^{\mu\nu}(\vec{x}) = 4\int \frac{T^{\mu\nu}(\vec{x}')}{|\vec{x} - \vec{x}'|} d^3x' \tag{2.6}$$

or after employing the large distance ($r \equiv \vec{x} - \vec{x}' \gg \vec{x}'$) approximation,

$$h^{\mu\nu} = \frac{4}{r}\int T^{\mu\nu} d^3x' \tag{2.7}$$

Based on our initial linearization, we can say that $\frac{\partial T_\mu^\nu}{\partial x_\nu} = 0$ (but note that these are just the classical conservation laws). From this and Gauss' theorem, we can rewrite Eq. 2.7 as

$$h^{\mu\nu} = \frac{2}{r}\frac{d^2}{dt^2}\int x^\mu x^\nu \rho(\vec{x}) d^3x = \frac{2}{r}\frac{d^2}{dt^2} I^{\mu\nu}. \tag{2.8}$$

Equation 2.8 says that the amplitude of gravitational waves is inversely proportional to the distance from the source, and is proportional to the acceleration of the quadrupole moment of the rest-mass density ($I^{\mu\nu}$). It may be insightful to note, that no lower-order moments *could* contribute to

[4]While a differential analysis of the two polarizations is key to extracting physical parameters from gravitational wave signals, we are presently interested in the overall gravitational wave strain h.

gravitational radiation, as the first-moment (monopole) is the total mass of the system, which is constant; and the second (dipole) is the center of mass of the system, which is inertial.

Combination of Eq. 2.8 and the exact form of Eq. 2.5 (Peters & Mathews, 1963) yields an equation for the power dissipated per solid angle α:

$$\frac{dP}{d\alpha} = \frac{G}{8\pi c^5}\left(\frac{d^3}{dt^3} I_{\mu\nu}\hat{e}_{\mu\nu}\right)^2 \tag{2.9}$$

It is then trivial to plug in the quadrupole moment of a binary system (see the equations presented in §A.3), integrate over all angles, and average the power dissipated over a period to obtain

$$<\mathrm{P}> = \frac{32G^4}{5c^5}\frac{M_1^2 M_2^2 (M_1+M_2)}{a^5(1-e^2)^{\frac{7}{2}}}\left(1+\frac{73}{24}e^2+\frac{37}{96}e^4\right) \tag{2.10}$$

In Eq. 2.10, the strong dependence on eccentricity is reasonable given its enhancement to the acceleration at pericenter where the majority of the power will be dissipated; note that this has a tendency to circularize the orbit[5]. Peters (1964) derives an equation for the loss of angular momentum; the effect on eccentricity is given by

$$\left\langle \frac{de}{dt} \right\rangle = -\frac{304G^3}{15c^5}\frac{M_1^2 M_2^2 (M_1+M_2)}{a^4(1-e^2)^{\frac{5}{2}}}\left(e+\frac{121}{304}e^3\right) \tag{2.11}$$

Plugging into Eq. 2.8 (e.g. Postnov & Yungelson, 2006) gives the strain of each polarization,

$$h_+ = \frac{2G^{\frac{5}{3}}}{c^4}\frac{1}{r}(\pi f \mathrm{M})^{\frac{2}{3}}\mu(1+\cos^2 i)\cos(2\pi f t) \tag{2.12}$$

$$h_\times = \frac{4G^{\frac{5}{3}}}{c^4}\frac{1}{r}(\pi f \mathrm{M})^{\frac{2}{3}}\mu\cos i\sin(2\pi f t) \tag{2.13}$$

where we have introduced the inclination i at which the system is being observed (s.t. $i = \frac{\pi}{2}$ is a system edge-on), and frequency and phase f and t. Thus if the coalescing binary is perpendicular to the direction of the observer, one of the polarizations is null—greatly reducing the extractable information from the inspiral signal.

The 'chirp-mass' $\mathcal{M} \equiv \mu^{\frac{3}{5}} M^{\frac{2}{5}}$, is commonly used in the literature as it fully determines the GW amplitude for a given distance and frequency. Using the chirp-mass, and averaging over an

[5]Relativistic beaming has the same effect, but is only especially important at the very last moments of in-spiral, where, especially for DBH systems, it can deliver a strong kick (e.g. Campanelli et al., 2007).

orbital period, the wave amplitude can be written as

$$h = \left(\frac{32}{5}\right)^{\frac{1}{2}} \frac{(G\mathcal{M})^{\frac{5}{3}}}{c^4} \frac{(\pi f)^{\frac{2}{3}}}{r} \tag{2.14}$$

or in more convenient units, as

$$h = 10^{-22} \left(\frac{\mathcal{M}}{M_\odot}\right)^{-\frac{5}{3}} \left(\frac{f}{100\text{ Hz}}\right)^{\frac{2}{3}} \left(\frac{r}{100\text{Mpc}}\right)^{-1} \tag{2.15}$$

The 'strain' (Eq. 2.15)–the fractional change in distance as a gravitational wave passes a detector–is what would actually be observed by detectors; with a characteristic value around 10^{-22}–10^{-21}.

We can similarly rewrite the expression for average power (Eq. 2.10) as a function of the chirp-mass, and the frequency of the system

$$<\text{P}> = \frac{32G^{\frac{7}{3}}}{5c^5}(\mathcal{M}\pi f)^{\frac{10}{3}} \tag{2.16}$$

Equation 2.10 can be directly employed with Eq. A.3 (§A.3) to find the evolution of the semi-major axis

$$\left\langle \frac{da}{dt} \right\rangle = -\frac{64G^3}{5c^5} \frac{M_1^2 M_2^2 (M_1 + M_2)}{a^3(1-e^2)^{\frac{7}{2}}} \left(1 + \frac{73}{24}e^2 + \frac{37}{96}e^4\right) \tag{2.17}$$

We can now determine how long it will take a binary of reduced mass μ, period τ, eccentricity e, and total mass M to merge due to gravitational radiation. In convenient units (Hughes, 2009)

$$\tau_{\text{merge}} \approx 5 \times 10^{10}\text{ yr } \left(\frac{\tau}{\text{day}}\right)^{\frac{8}{3}} \left(\frac{\mu}{M_\odot}\right)^{-1} \left(\frac{M}{M_\odot}\right)^{-\frac{2}{3}} (1-e^2)^{\frac{7}{2}} \tag{2.18}$$

This is the nature of the orbital decay predicted for PSR1913+16, and its consistency with observations, illustrated in Fig. 1.1. With a baseline-reference the diameter of the earth, a standard GW strain amounts to a change of about 0.01 pm–one billionth the width of a human hair. This should be detectable with current laser-interferometer gravitational wave detectors.

2.2 Gravitational Wave Observatories

The first attempt at a gravitational wave detector was with the resonant-mass type design—termed a "Weber bar" after its creator (Weber, 1960, 1968). A network of such resonant-mass detectors are currently operational (Prodi et al., 2000). Currently the instrument of choice is consistently

the the Michelson interferometer (see, e.g. Michelson, 1924), pioneered in large part by Weiss and Forward (Moss et al., 1971; Weiss, 1972). None the less other strategies, such as pulsar-timing arrays are being explored. Diagrammed schematically in Fig. 2.1, The Michelson interferometer offers a natural method of increasing the effective detector size by repeatedly reflecting the laser beam along each beam cavity. While pulsar timing arrays utilize the entire path length between observer and pulsar, interferometers suffer from better understood and well constrained noise sources.

As a gravitational wave crosses the detector, the strain pattern expands space—and any equipment occupying it—in one direction, while contracting it in the perpendicular direction. The effective difference in path length traversed by the laser-beam is minuscule, only one part in $\sim 10^{21}$. The Michelson interferometer uses a beam-splitter to pass incident laser light along two perpendicular paths, at the end of which they are reflected back. In the unstrained state (devoid of GWs) the lasers from the two paths interfere destructively at the antisymmetric port which then sends no output signal. When a GW passes through the apparatus, one arm of the detector will be expanded and the other contracted–leading to constructive interference at the antisymmetric port, and an output signal proportional to the strain and the input laser intensity. Three interferometers constitute the LIGO system, one 4 km and one 2 km interferometer are located at Hanford, Washington; and one 4 km-long is located in Livingston Parish, Louisiana, shown in Fig. 2.2. Data is compared between the two LIGO sites, and also the GEO and VIRGO instruments, allowing for better noise and error rejection.

Our discussion of detector design follows Abbott et al. (2009), and is thus based on the LIGO design. All of the other currently operating laser-interferometer GWOs operate on the same principles, however. To increase the detector sensitivity, a Fabry-Perot optical cavity reflects the light back-and-forth along the arms to increase its power and effective length; this affects a factor of 100 increase in sensitivity. Additionally, another power recycling cavity is established by the Power Recycling Mirror. Combined, the power recycled Fabry-Perot configuration yields an 8000 times increase in sensitivity.

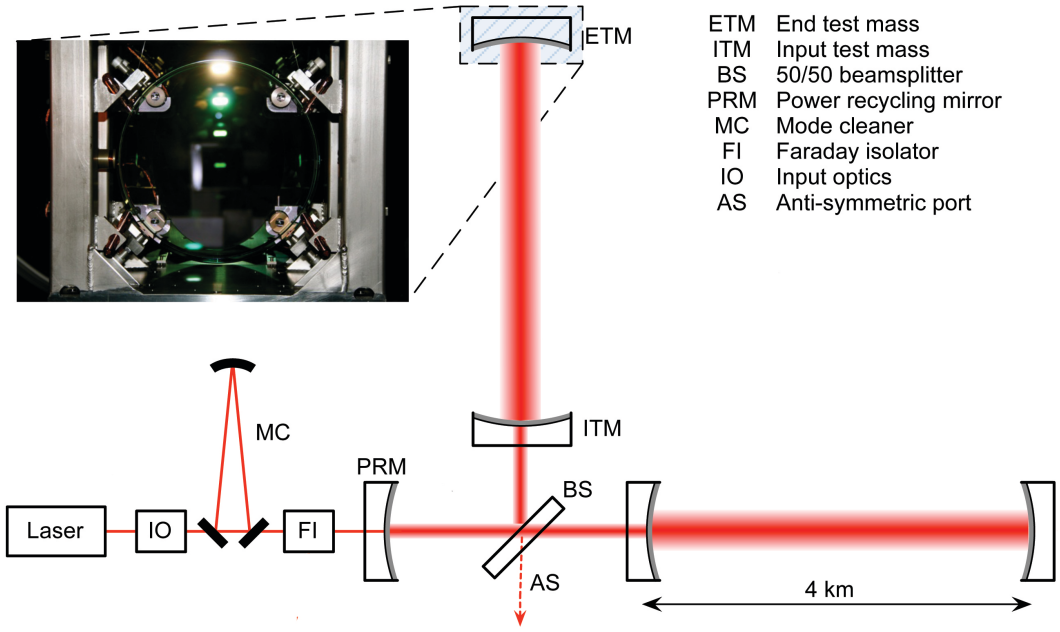

Figure 2.1: LIGO Michelson Interferometer–modified from Abbott et al. (2009). This configuration establishes a Fabry-Perot cavity between each ITM and ETM, and a power recycling cavity between the PRM and each ITM. The combined effect of these cavities is an $\sim$ 8000 times increase in sensitivity compared to a simple Michelson interferometer. The inset shows an ETM mirror inside its pendulum and seismic isolation system. Although the mirror is transparent in the visual spectrum, it is highly reflective in the infrared band of the laser. The mirror actuators are also apparent around the perimeter.

Despite fused-silica optics, polished to a surface deviation of less than 5Å, numerous measure are taken to eliminate as much noise as possible. The mode-cleaner filters laser noise before passing the light into the vacuum cavity, which is kept at a pressure of $\leq 10^{-8}$ torr; despite the high vacuum, baffles are used along the beam path to catch scattered light. A Faraday isolator uses the Faraday effect[6] to ensure only source light enters the system (Gauthier et al., 1986). Even the small amount of absorbed light causes minor thermo-elastic distortion of the mirrors, and thus additional lasers ('heating beams') are used to control the radial profile of the mirrors.

Noise reduction is critical to Interferometric GWO operation, as sensitivity to signals smaller than even (e.g.) the stochastic seismic background is required. Vibrational isolation is

[6]Light from the source is polarized vertically, then passes through a magnetic field rotating the polarization 45° until an analyzer on the opposite end allows light of that polarization to pass through. Light entering in the opposite direction enters the rotation chamber at 45° from vertically, and is *further* rotated 45°–becoming horizontal–once it reaches the opposite end, where it is completely absorbed.

Figure 2.2: LIGO Livingston, Louisiana Detector–Reproduced from Abbott et al. (2009).

provided by four-layer mass-spring isolation stacks, to which the pendulums which house the optics are attached. Between the optics and the pendulum, electromagnetic actuators actively damp eigenmodes of the suspension system and also maintain proper cavity length. Currently, one detector location also employs hydraulic seismic pre-isolators.

Overall, LIGO is sensitive to signals between 40-7000 Hz, with a peak sensitivity of 3×10^{-23} rms strain-noise at $\sim$ 100 Hz. Figure 2.3 shows detector sensitivity over the frequency band. The expected detection rates for these sensitivities and those of the 'Advanced LIGO' improvements–scheduled for operation in 2015 (Abadie et al., 2010)–are shown in Fig. 2.4 as a function of initial stellar-mass fraction—one of the most uncertain factors in calculating rates, and thus providing the full range of possible results. The detectors themselves are only the first step in truly detecting events. DCO in-spirals will appear as 'bursts' in the data, with durations of less than a second. These bursts must be dredged out of months or years of observations from five or more detectors (e.g. Virgo-LIGO-GEO coincident runs). Also, because the event rate per distance is limiting, the most likely signal-to-noise ratios (SNR) will be at or just-above threshold.

To monitor and calibrate the efficiency and efficacy of the data analysis procedures, simu-

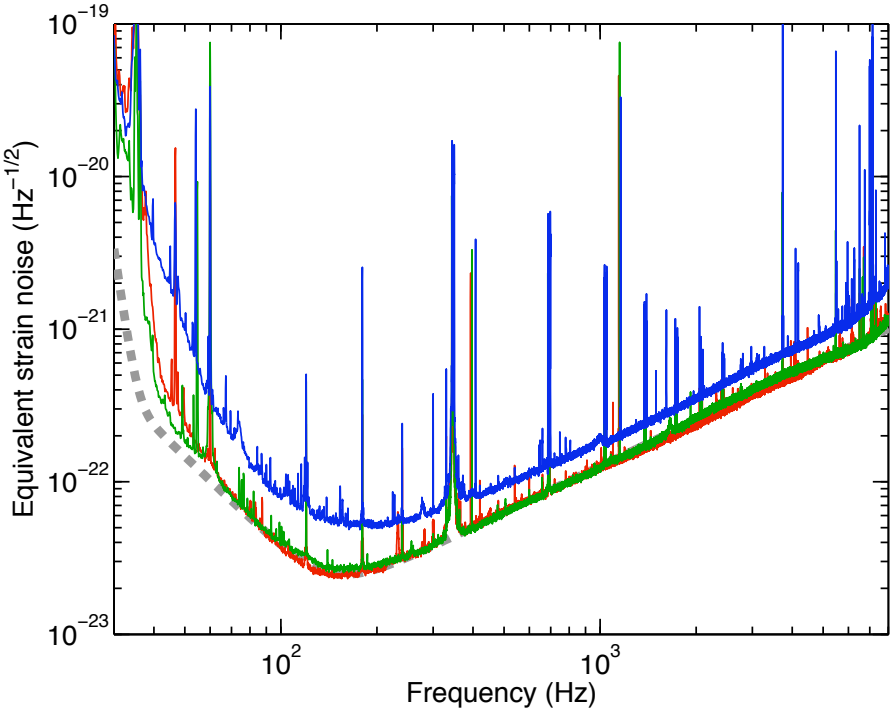

Figure 2.3: LIGO Frequency Sensitivity–Reproduced from Abbott et al. (2009). Each of the three MI are shown, with H1 in red, H2 in blue, and L1 in green. The dashed grey line corresponds to the design goals.

lated events are 'injected' both via software and hardware–in which simulated GW signals are added via the test-mass actuators. Overall excess power algorithms are preferred over templates due to both the large parameter space that would need to be analyzed, and also the insufficiency of the post-newtonian algorithms which are predominant in current simulations.

The purpose of GWOs like LIGO is not merely to make a detection, but to gleam new information from their sources via parameter reconstruction—which, in itself, is a highly complex task. Theoretically, the chirp-mass, semi-major axis and distance to the object should be readily accessibly from the in-spiral waveform (see §2.1 and particularly Eqs. 2.14 and 2.17; note that the eccentricity will be assuredly approximately zero). The angular position of the event could be determined to some accuracy by the difference in detection time from numerous detectors. Based on timing alone, three detectors could determine a unique position per hemisphere, with a fourth detector needed to remove the degeneracy across the plane (measurement of each wave polarizations

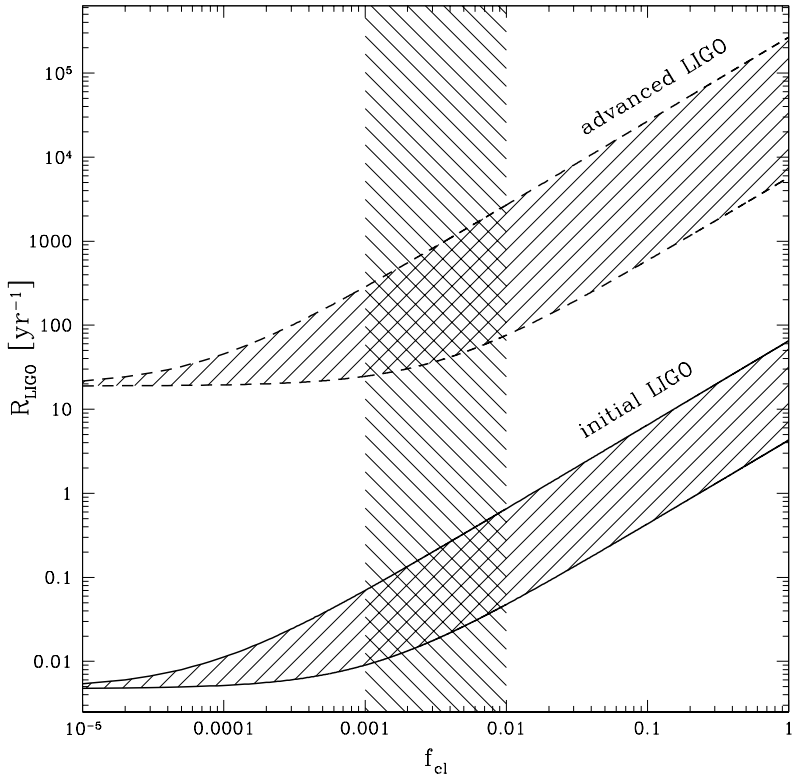

Figure 2.4: Expected Detection Rates for Current and Advanced LIGO–reproduced from Sadowski et al. (2008). The detection rate is shown as a function of the initial stellar-mass fraction in dense star clusters–the most likely range of which is represented in the shaded region. The upper and lower rate bounds are from estimates on cluster merger rates–for more details see Sadowski et al. (2008) and references therein.

however, could resolve that degeneracy with only three detectors). This suggests a realm of astronomy the exact reverse of the classical, photonic regime in which angular position can be resolved to extreme accuracy, and distance can only be determined approximately by inference and relation to an elaborate 'ladder'-scheme.

Accurate measurements of these parameters would be valuable for the advancement of astronomical knowledge; many applications have been suggested, from better determining the Hubble constant (e.g. Schutz, 1986), to better constraining NS equations of state (e.g. Krolak & Schutz, 1987). Parameters which influence the frequency-space evolution[7] of the signal can be determined to an accuracy proportional to $\sim \mathcal{N}_{\rm p}^{-1}$, where $\mathcal{N}_{\rm p} \sim 10^3$–$10^4$ is the number of periods for which the

[7]Namely the phase evolution which requires waveforms accurate to much higher order than those described in §2.1

signal is detectable (e.g. Finn & Chernoff, 1993; Cutler & Flanagan, 1994). Information encoded in the amplitude and polarization, on the other hand, will simply be inversely proportional to the SNR (ρ), or for numerous detectors, the cumulative SNR ($\rho = \left[\Sigma\rho_i^2\right]^{\frac{1}{2}}$).

For the purpose of the current study, we are concerned with reconstruction of the source distance and angular position in the sky. Fairhurst (2009) and Cavalier et al. (2006) suggest that in a 3-detector network, using only timing information (for a lower bound on accuracy), the source could be triangulated to 1–20 square degrees. These results are consistent with earlier work by Cutler & Flanagan (1994), suggesting an angular and distance uncertainty of $\sigma_\alpha \sim 1^\circ$ and 30% respectively. The possible addition of a fourth interferometer, such as a possible AIGO detector in Australia or LGCT in Japan, could significantly enhance the sky localization accuracy and moderately improve distance sensitivity (Mandel, 2010; Fairhurst & Mandel, 2011).

Preparation for the next generation of gravitational wave observatories is already underway, for instance the space-based Laser Interferometer Space Antenna (LISA) (e.g. Belczynski et al., 2008). This detector, in solar orbit with millions of kilometer long arms, would have accuracies orders of magnitude higher than LIGO-Virgo, and a sensitivity band extending much lower. LISA could potential detect GW from relatively stable, large-period binaries as well as the inspiral of SMBH(e.g. Willems et al., 2008). The use of atomic interferometers, currently used to make high precision measurements of fundamental constants (e.g. Fixler et al., 2007; Zhou et al., 2011), is also being explored (e.g. Dimopoulos et al., 2009). In terms of non-interferometric designs, 'MiniGrail' (e.g. Gottardi, 2007) is being developed as a next-generation resonant-mass detector. Current prototypes by the MiniGrail group are able to achieve strain sensitivities of order $\sim 10^{-20}$.

3 Simulation and Selection

Previous studies of the distribution of double compact objects have generally used static simulations of only the Milky-Way's current gravitational potential (see §I). From those simulations the overall distribution of DCOs has been generalized to all galaxies from which GW signals might be detected. While this approach is a logical starting point, it is lacking in numerous fundamental features. Most fundamentally, GW Signals are expected from a sample volume including at least hundreds of galaxies with morphologies and histories which can vary significantly from that of the Milky-Way (MW). Even in the case of the MW alone, however, the current mass is significantly larger than its effective mass over cosmological time-scales. Use of the current MW mass will tend to over-retain DCOs which might otherwise become unbound. Finally, the morphology of galaxies is strongly dependent on the history of their mergers and evolutionary environment. Tidal interactions and collisions between galaxies can have a strong impact on the distribution of high velocity DCOs—an effect entirely absent from analysis of single, static halos.

To address these concerns and improve upon previous models, we use full cosmological structure formation simulations to elucidate the distribution of double compact objects. Most studies to date have only explored the radial distribution of binaries relative to their host. The inherently large-scale nature of our simulations allow us to examine the full, three-dimensional phase-space distribution of systems for many host masses and evolutionary histories. In §4 we discuss the results of these simulations which elucidate the additional information to be eventually compared with GW observations. In this section, we describe the key feature of our simulations[1].

[1]See Zemp et al. (2009) for a detailed description.

3.1 Dark Matter Simulation

The simulation is composed of 256^3 dark-matter (DM) particles in a periodic, 80 Mpc co-moving cube. In the cosmological size-scale of interest, Baryonic-matter (e.g. stars and gas) is relatively insignificant (Jarosik et al., 2011). The mass resolution is $m_p = 1.07 \times 10^9\ M_\odot$, or roughly 2000 particles per Milky-Way like halo. Our simulations are thus sensitive to the distribution of dwarf-halos and larger structures, and most importantly the merger-history of larger (MW-like and above) halos.

The simulation is initialized at redshift $z = 22.4$ (13.5 Gyrs ago, $t \approx 161$ Myr after the big-bang), and seeded with density perturbations and appropriate cosmological parameters from the Wilkinson Microwave Anisotropy Probe third-year (WMAP3) data (Spergel et al., 2007)—namely, a Hubble factor of $H_0 = 73$ km s^{-1}, a matter energy density of $\Omega_{M,0} = 0.238$, and a dark energy density of $\Omega_{\Lambda,0} = 0.762$ (see table 3.1 for a summary of key simulation parameters). These values are still consistent with the most recent results of WMAP7 (Larson et al., 2010; Jarosik et al., 2011). Periodic boundary conditions increase the effective size of the simulation, allowing data to be analyzed to a radius of 80 Mpc from any origin. Particles are never counted repeatedly to avoid artificially polluting the distribution's power spectrum.

Feature	Value
Size (comoving)	80 Mpc
Initialization Time	161 Myr (z = 22.4)
$\Omega_{M,0}$, $\Omega_{\Lambda,0}$	0.238, 0.762
Particles	$256^3 \approx 17 \times 10^6$
Mass Resolution	1.07×10^9 M$_\odot$
Populated Halos (z=1.6)	2461
Tracers per Populated Halo	2000

Table 3.1: Summary of Simulation Values.

The simulation is evolved using the parallel tree code PKDGRAV2 (Stadel, 2001) until $z = 1.60$ (4.24 Gyr)–the star formation peak (Madau et al., 1996). At this point, halos are identified using a friend-of-friends algorithm in which all particle pairs are linked if their separation is less than a certain fraction of the mean particle separation (Davis et al., 1985). Each halo with mass greater than $2.15 \times 10^{11} M_{\odot}$ (2461 halos) is populated with 2000 massless tracers, each representing a compact binary system (hence-forth we use the term 'tracer' to describe a simulated DCO). Tracers are injected into the center of their halo, with an isotropic Maxwell-Boltzmann velocity distribution with mean speeds $\bar{v} = 360$, 180, & 90 km s^{-1} and dispersions $\sigma_v = 150$, 75, & 37.5 km s^{-1} for models M_{360}, M_{180}, & M_{90} respectively; summarized in table 3.2 and consistent with the observed distribution of systemic velocities (see §1.3).

Model	Mean Velocity (km s^{-1})	Variance (km s^{-1})
M_{360}	360.0	150.0
M_{180}	180.0	75.0
M_{90}	90.0	37.5

Table 3.2: The mean velocity and variance of each kick-velocity model. Tracer velocities are initialized isotropically according to a Maxwell-Boltzmann distribution, in accordance with observations (see §1.3).

Figure 3.1 shows a small, characteristic region of the simulation. Tracers are shown in green, red, and blue corresponding to models M_{360}, M_{180}, & M_{90} respectively, overlaying the dark matter distribution in white. Some dwarf halos (bottom right quadrant) are apparent which weren't massive enough to be populated with tracers.

The small length scales in the very centers of halo cores (distances less than tens of kpc—corresponding to regions smaller than the blue tracer cores in Fig. 3.1) are not adequately resolved in our simulations, and the length scales of interest are significantly larger—on the order of tens of Mpc. Additionally, baryonic matter is expected to dominate in these local regions, thus any DCOs which are entirely bound to halo cores can be expected to virialize with the local stellar distribution.

Tracers are weighted linearly with their progenitor halo's mass in all of our calculations, as

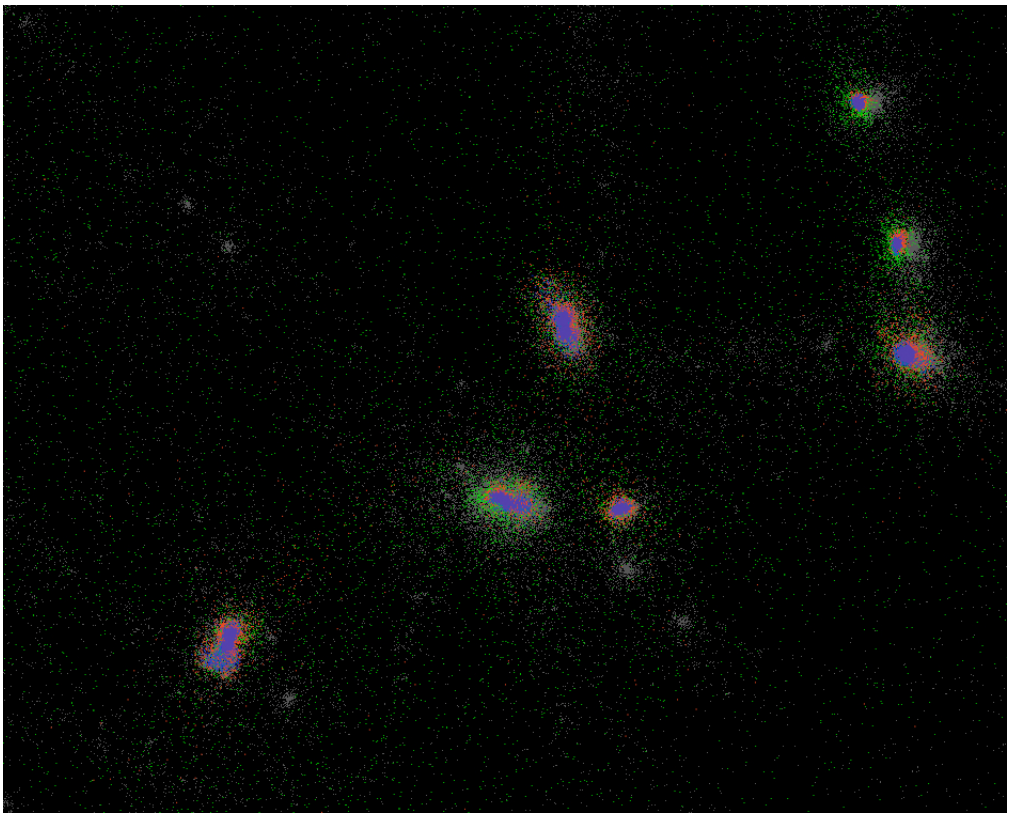

Figure 3.1: Snapshot of a small at z = 0 region of the simulation. Tracers (colored) of different velocities are overlaid with dark matter (white). The colors green, red, & blue correspond to models M_{360}, M_{180}, & M_{90} respectively.

the star formation rate is close to linearly related to stellar mass (Shimasaku et al., 2008; Dutton et al., 2010)–illustrated in Fig. 3.2–roughly as is the relation between stellar mass and halo mass over large mass ranges (Moster et al., 2010). In general, the local merger rate of DCOs is given by the convolution of the star formation rate with the probability distribution of merger time delays. As described above, we use the approximation of a single injection time, and perpetuate all tracers until redshift zero. The merger of systems formed near the star formation peak dominate the local merger rate by a factor of $\gtrsim 3$ (Guetta & Piran, 2005), motivating our simplification. Additionally, merger times are found to be relatively insensitive to kick velocity (e.g., Bloom et al., 1999). Thus, for each of our kick-velocity models, our results can be easily scaled to match the expected merger rate of a given model.

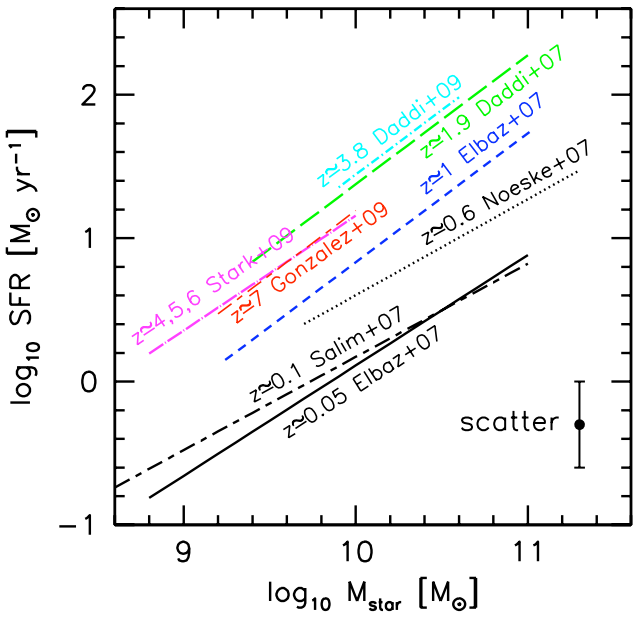

Figure 3.2: Star Formation Rate (SFR) vs. Stellar Mass–reproduced from Dutton et al. (2010), summarizing data from references therein. Across a broad range of red-shifts, the SFR is close to linearly proportional to a halos stellar mass. We therefore weight our tracers linearly with the mass of the halo they were formed in.

3.2 Local Group Selection

In §3.1, the draw backs of simulations involving only a Milky-Way like halo were discussed, and in §3.1 the improvements in the current simulations were described. To better model the local-universe from which observations will be made, we have selected a region of the simulations which is maximally similar to our region of the universe.

As described by Zemp et al. (2009), a fixed MW halo potential tends to noticeably overestimate the bound population of tracers. Additionally, the nascent environment of a given tracer has a drastic effect on its evolution, as seen in Fig. 3.3. The history of mergers and tidal interactions between halos is similarly important for determining how well tracers are bound to their progenitor halos over time. We use the current properties of the local universe to best match an appropriate region of the simulation. Specifically, a local-like universe is defined by criteria modified from Hoffman et al. (2008):

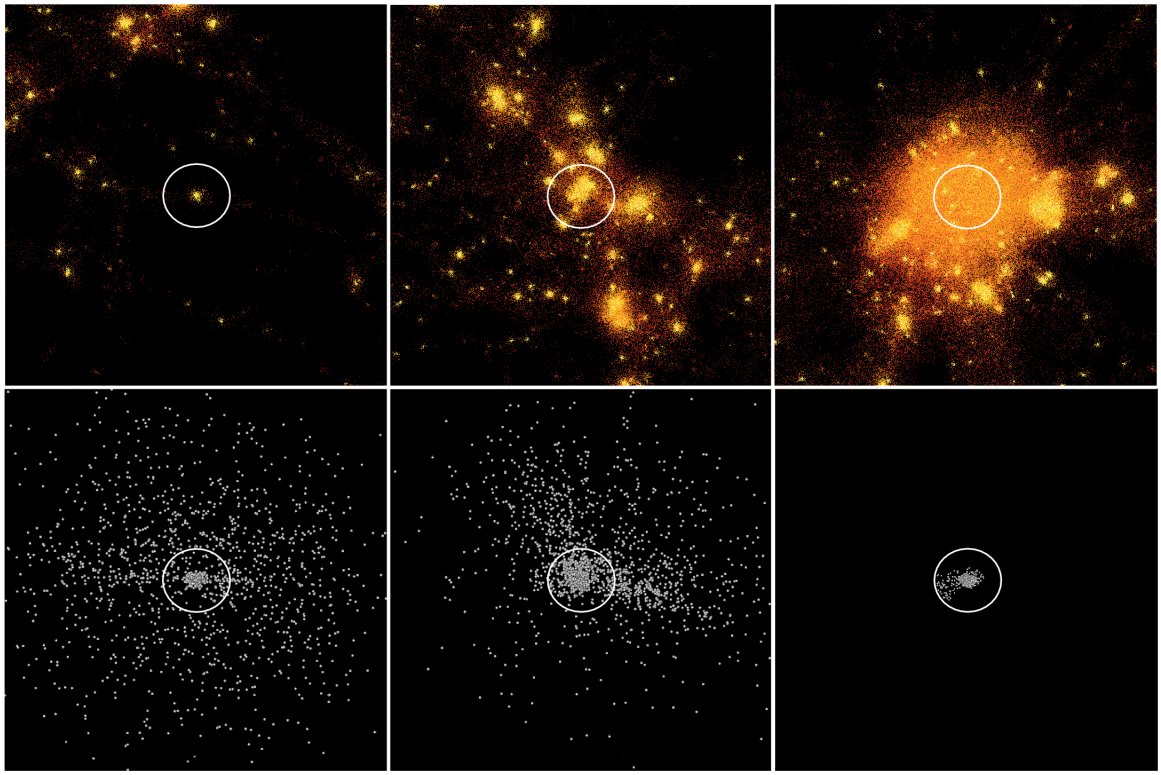

Figure 3.3: Simulation at z = 0.0 with Dark Matter (top row) and Tracer (bottom row) distributions in a variety of environments–reproduced from Zemp et al. (2009). The tracers in each bottom panel correspond to their progenitor dark matter halos circled in the top panel directly above. All three pairs displayed are from the highest kick-velocity scenario (M_{360}). In the cluster environment (rightmost panel), even high kick-velocities are small compared to escape velocities approaching 1000 km s^{-1}. Each panel is 10Mpc in length.

1. Two dark matter halos with maximum circular velocities $v_c \in [125, 270]$ km s^{-1}
2. These halos separated by a distance $d \leq 1.4$ h^{-1} Mpc
3. Relative velocities $v \leq 0$ km s^{-1}
4. No halos with higher maximum circular velocities than either of the pair within 3 Mpc.
5. There is a virgo-like halo with $v_c \in [500.0, 1500.0]$ km s^{-1} and $d \in [5.0, 12.0]$ h^{-1} Mpc,
6. No other large halos with virgo-like masses within 12 h^{-1} Mpc.

While this local-like universe doesn't perfectly parallel the true history and environment of the milky-way and its surrounding region, we assume that similar resulting characteristics will be

indicative of similar pasts and kinematics. Small incongruities between the simulated and true local universe should be insignificant in the large volumes under consideration.

Out of the 2461 dark-matter halos populated with tracers, there exist tens of pairs matching criteria 1 and 2—only two of which have virgo-like clusters at the appropriate distances. One of these two groups has additional massive structures at virgo-like distances, and was therefore excluded based on criteria 6. The resulting, optimal local-like group is depicted in Fig. 3.4. The Milky-Way and Andromeda analogs are circled on the left, and the virgo-like cluster on the right. For completeness, our distributions in §4 are all generated from a Sol-like offset from the MW center, relative to the M31-equivalent galaxy.

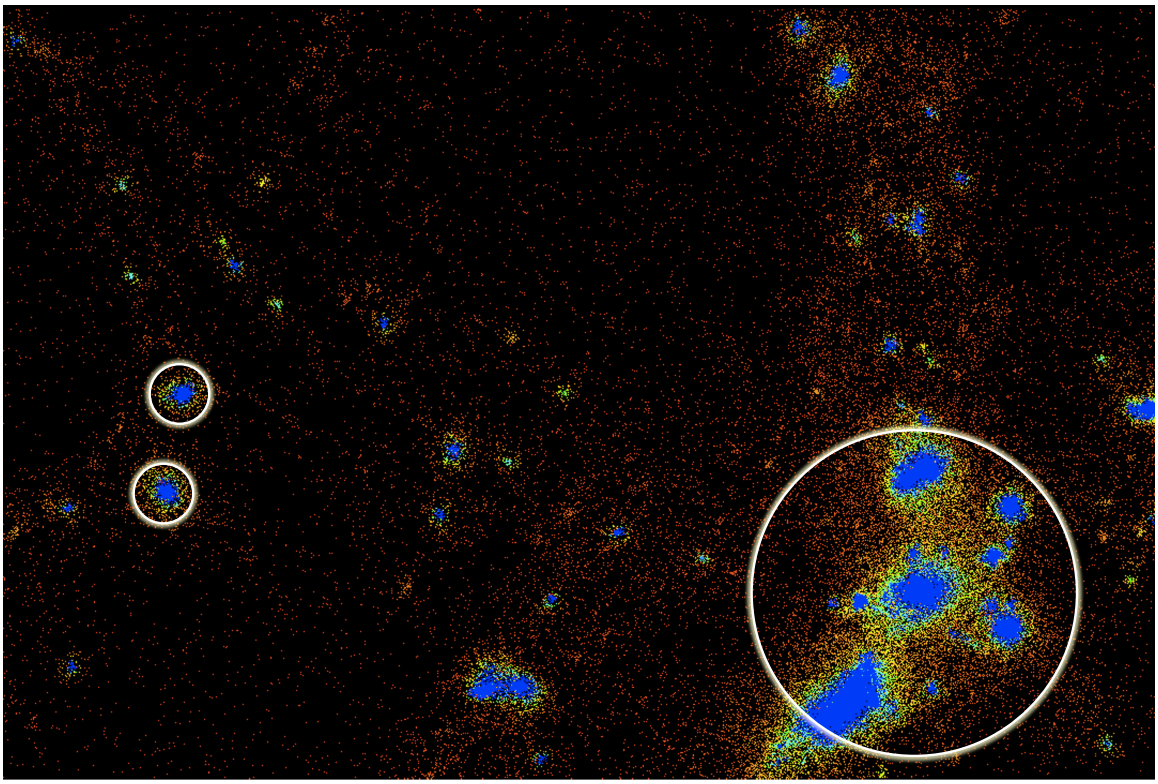

Figure 3.4: The local group analog in projection: Milky-Way and Andromeda-like halos circled on the left, and virgo on the right. This $\sim$ 10 Mpc wide region is colored by density.

Part II

Results

4 Particle Distributions

Figure 4.1 shows the local-like universe described in §3.2—the density profile juxtaposed with the tracer distributions for each kick-velocity model (described in §3.1). The most apparent feature of Fig. 4.1 is the extension of the tracer distribution at high velocities (360 km s^{-1}), consistent with predictions. A comparison of the region around the virgo-like cluster (right side) with that of the MW-like pair (left side) echos the results of Zemp et al. (2009) in regards to environment dependence. Because the potential well of the virgo-like cluster is far deeper than that of the pair, fewer tracers become entirely unbound. At the same time, the tracers from each halo of the cluster have become significantly mixed, and even the tracers which are contained in the inner halo-cores of M_{90} are extended into the outer-halos of M_{360}.

Tracers at velocities above the escape velocity of their progenitor halo become unbound, and form an extended background. Double compact objects which fall into this group could be expected to merge at significant distances away from their hosts. DNS and BH-NS systems are expected to produce large electromagnetic outbursts shortly after the peak of their GW-inspiral signals; including, perhaps, short-duration Gamma-Ray Bursts (GRBs) (see, e.g. Lee & Ramirez-Ruiz, 2007). So far, short GRB host identifications have been based entirely on angular nearest-neighbor associations, as they themselves yield no known distance or red-shift information. As GRBs are believed to have been observed out to redshifts of a few, if their progenitors are distributed in a manner consistent with M_{360}, the probability of coincident associations could be non-negligeable.

These tracer distributions are quantified in Fig. 4.2, where mass is plotted as a function

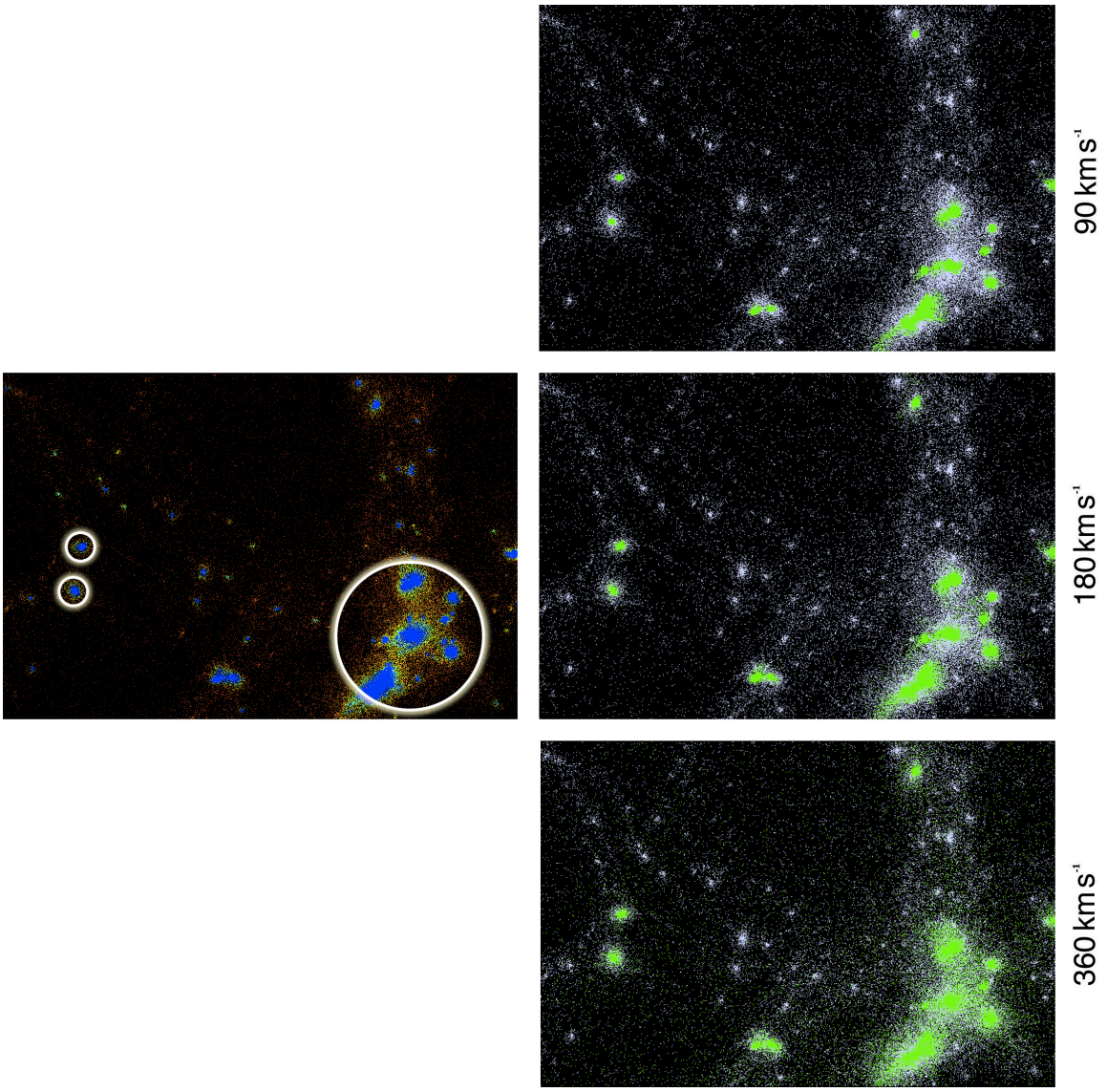

Figure 4.1: The Local Group Analog: Milky-Way and Andromeda-like halos, and Virgo-like Cluster indicated (Left Panel), and Tracers at Three Kick Velocities (Right Panel). The effects of kick on forming a DCO background are readily apparent.

of distance from the Milky Way-equivalent halo. The distribution of tracers are plotted for each velocity model—M_{90}, M_{180}, & M_{360}—from top to bottom. Although the tracer density peaks are only subtly altered, once the kick-velocity becomes comparable to the escape velocity of individual halos–e.g. $\sim$ 540 km s^{-1} for the milky way (Smith et al., 2007)–a fraction of tracers leave their progenitor potential wells. M_{180} (middle panel) shows the growth of 'skirts' around the primary distribution, but only in M_{360} (lowest panel) does a significant tracer background form.

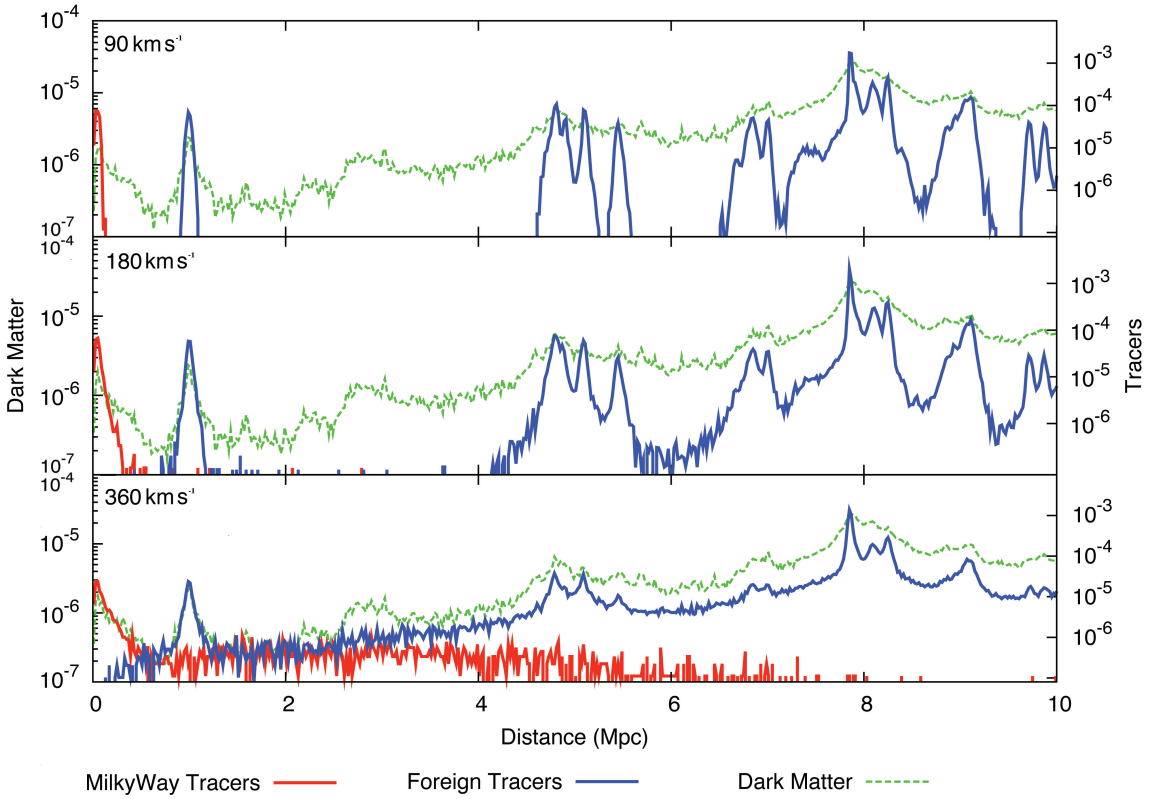

Figure 4.2: Radial Distribution of Tracers and Dark Matter for three Different Kick Velocities. Integrated particle mass in uniform radial-width shells is plotted versus distance from a Sol-equivalent offset from the Milky Way center. The y-axis is given in arbitrary simulation units, and can easily be scaled to any population synthesis model. As the kick-velocity increases from 90 km s^{-1} (top panel) to 360 km s^{-1} (bottom panel) a noticeable portion of tracers becomes delocalized, forming a background and mixing populations.

In these simulations, tracers only respond gravitationally, and therefore their dynamics are akin to that of a dark-matter test particle. In the lowest velocity case, thus our tracers exactly follow the central DM peaks. On scales below the resolution of this simulation, double compact objects would be expected to follow the more effectively damped baryonic matter distribution. Higher velocity tracers, on the other hand, escape their halos—and regions of significant baryonic matter. In such extended intergalactic regions DCOs would only interact gravitationally, and thus be expected to follow distributions similar to that of DM in the same region. This behavior can be clearly seen in M_{360} of Fig. 4.2, where the tracer skirts now follow the overall DM distribution, instead of only the DM over-densities as in M_{90} and M_{180}.

The relative portion of tracers in the emerging background of the MW-like halo are depicted in fractional cumulative distribution in Fig. 4.3. The dashed black-line (and second y-axis) shows the cumulative distribution of dark-matter to illustrate the local structure. The number of tracers

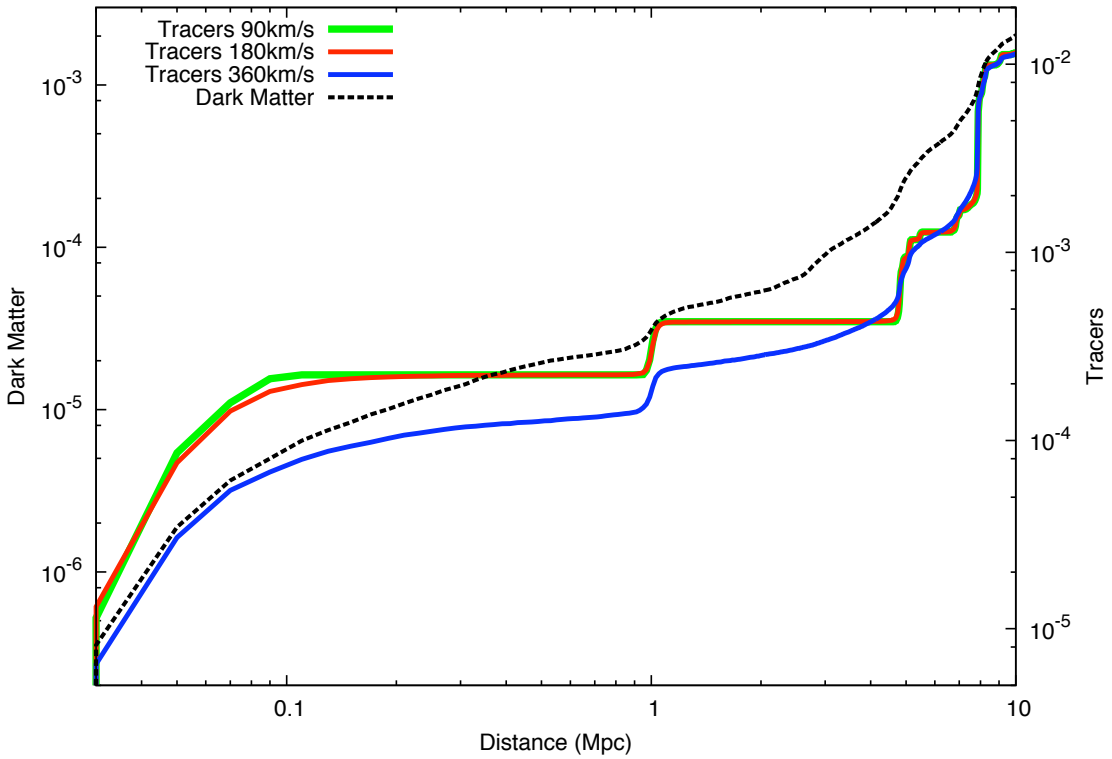

Figure 4.3: Cumulative Distribution of Dark Matter and Tracers for Three Kick Velocites. Although the number of tracers in the central halo is noticeably lower for the highest kick-velocity model, the difference is negligible once the volume reaches the Virgo-like cluster, where the background distribution of tracers outweighs changes in local distributions. The rate of mergers is directly related to these results, with a proportionality constant describing how the merger rate scales with dark matter halo mass.

within a sphere encompassing the primary and secondary halos is noticeably depleted, but as the volume approaches the virgo-like cluster, the number of (sub)halos becomes large, and the central densities dominate the tracer fraction regardless of kick velocity.

As discussed in §1.4, significant attention has been given to the expected rate of GW-inspiral–and therefore, also predictions of the number of progenitors in a local volume (e.g. Sadowski et al., 2008). Figure 4.3 can be scaled to any of the results presented in §1.4. For an up-to-date review of expected merger rates, see Abadie et al. (2010). Despite the background of DCOs that

form from large kick-velocities, the majority of systems remain bound to their hosts, and differences are negligible beyond about 8 Mpc. Thus, the merger-rate of DCOs in a LIGO-Virgo detectable volume should be insensitive to kick-velocity.

Few studies have explored the projected distribution of DCOs in the sky, and the few which have (e.g. Podsiadlowski et al., 1995) suffer from the same restrictions listed in §3.1. The projected sky distributions of tracers and dark-matter from this study are plotted in Fig. 4.4. All particles of a given type within the labeled distance are projected onto a spherical surface with 2°x 2° bins. Each bin is then colored logarithmically by density, and mapped onto the plane. White pixels are those with tracer densities below the resolution of the simulations.

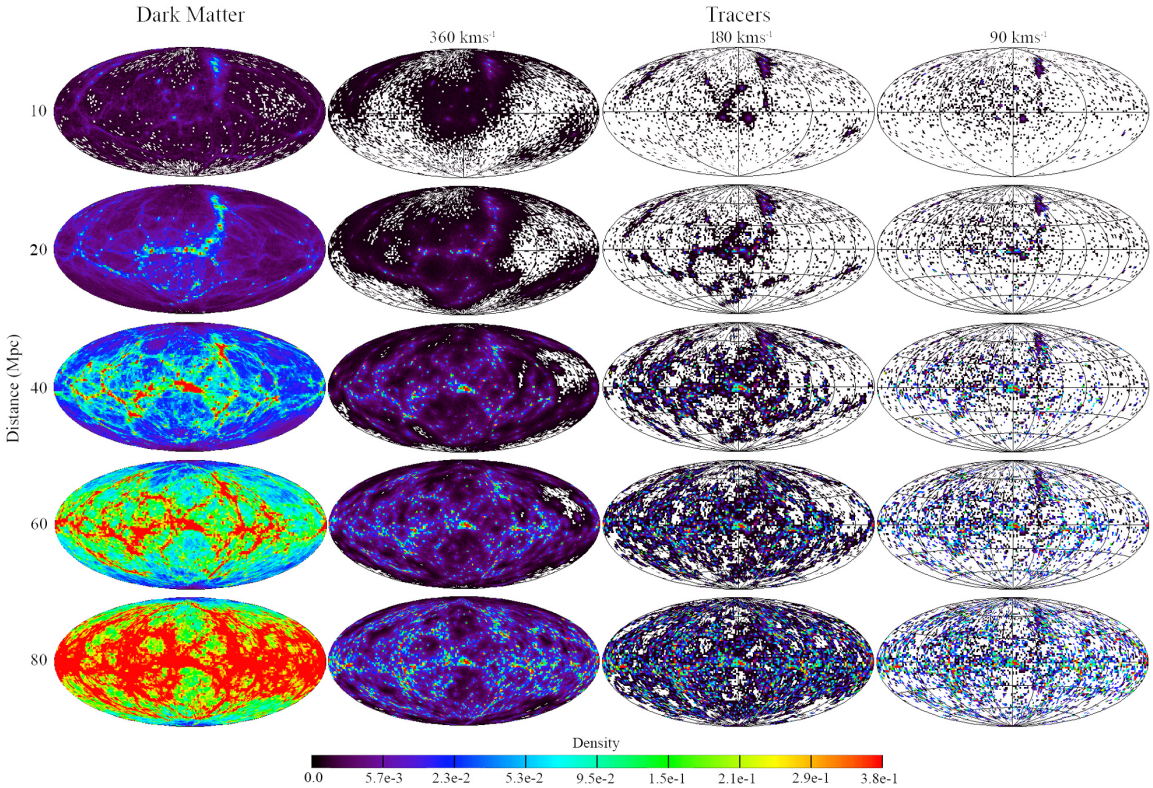

Figure 4.4: Sky Maps of Dark Matter and Tracers showing highest to lowest kick-velocity as a function of distance. Figures make use of Hammer equal-area projections with 2°x 2° bins, colored by logarithmic density. White pixels represent densities below the resolution of our simulations. Comparison of the highest and lowest natal kicks illustrate that while peak densities remain relatively unchanged, a strong DCO background forms from systems which escape their progenitor halos.

Although the integrated tracer distribution is dominated by the bound population (Fig. 4.3),

the angular distribution of tracers (Fig. 4.4) varies dramatically. It is again apparent that at 90 km s^{-1} the tracers follow only the dark matter overdensities, as does the distribution of light (gas and stars). At 360 km s^{-1} the tracer distribution becomes more isotropic—more closely following the overall distribution of mass. At 10 Mpc, $\sim$40% of the M_{360} DCO mass lies in pixels outside those of M_{90}; this number falls to 15% and 10% for 40 and 80 Mpc respectively–a trend as expected for increasing DM isotropy in projection.

These sky maps are resolved to 4 square-degree pixels, comparable to the expected accuracy of GW observatories. The apparent differences in distributions suggest that the different velocity models could be distinguished with a sufficient number of detections. Indeed, the limiting feature of making such distinctions is the expected rate of detections. None-the-less, in §**??** we demonstrate that the underlying source distributions could indeed be deciphered, offering the prospect of constraining the progenitors and their properties with GW detections alone.

5 Data Distinguishability

In §4 we produced three possible configurations of gravitational-wave source distributions. In this section, we discuss their distinguishability with an array of laser-interferometer GW observatories like that of the LIGO-Virgo network. The differences between models M_{360}, M_{180}, and M_{90} illustrated in Fig. 4.4 suggest that the degree of isotropy alone could be a strong indicator of the underlying source distribution, similar to the use of anisotropy in analyzing the cosmic microwave background. Such a method would require a detailed sampling of the underlying population, which is not feasible considering the LIGO-Virgo detection rates illustrated in §2.2, Fig. 2.4. Instead, we assume a detailed knowledge of the underlying dark-matter distribution to facilitate analysis of a smaller sample size[1]. A simple Bayesian framework is used to distinguish between kick-velocity models, similar to the approach used by Mandel (2010).

The ability to distinguish between natal kick-velocity would not only help shed light on the cryptic mechanisms which deliver those kicks, but also provide valuable information on the distribution of DCO lifetimes. With enough detections, even the depths of galactic potential wells could be explored, and the local DM distribution better constrained. It remains to be seen how many signals are required, and at what accuracies, to begin drawing out useful statistical information.

Reconstructing the source location from GW signals is a complex task, and error estimates for those reconstructions even more so (see Cutler & Flanagan, 1994, and references therein); especially in comparison to classical electromagnetic observations. The distance to the emission event could be determined to within a mean of 30% (Cutler & Flanagan, 1994), and the angular loca-

[1] In practice, comparisons would be made between GW signals and the light-distribution.

tion of the event to approximately $1 - 2^{\circ}$[2] (Cavalier et al., 2006). At first glance, better distance determination might be expected by simply comparing the chirp mass and signal amplitude (using Eq. 2.15). The signal amplitude, however, is fairly uncertain; while the frequency and phase information encoding parameters, such as the chirp and reduced masses, can be determined to within $\lesssim 1\%$ (e.g., Cutler & Flanagan, 1994).

As detections have yet to be made, the precise accuracy of parameter reconstruction has yet to be seen. In our analysis we explore three possible detector accuracies summarized in Table 5.1. These accuracies appear as Point-Spread Functions (PSF) in our analysis. The PSFs are assumed to be gaussian in each coordinate direction, characterized by standard deviations in distance, right ascension, and declination: $\sigma_{\rm high} = [5\%, 1^{\circ}, 1^{\circ}]$, $\sigma_{\rm med} = [30\%, 2^{\circ}, 2^{\circ}]$, $\sigma_{\rm low} = [50\%, 4^{\circ}, 4^{\circ}]$. These reflect different assumptions for the high, medium, and low accuracy of positional reconstruction for gravitational-wave detections.

	Standard Deviation in		
PSF Accuracy	Distance	Theta (deg)	Phi (deg)
High	5%	1°	1°
Med	30%	2°	2°
Low	50%	4°	4°

Table 5.1: Point-spread function parameters. Sampled data points are convolved with a PSF composed of a gaussian distribution with the given standard deviations in distance, theta, and phi.

The exact parameter-estimation accuracy will depend sensitively on the operational details of the detector network, for example, the relative sensitivity of individual detector locations and their calibration accuracy. Additionally, the specific features of individual events (e.g. their signal-to-noise ratio) and their relationship with the detectors (e.g. sky location and orientation of the binary) will also effect the accuracy with which parameters can be reconstructed. While each of our models are symmetric with respect to angle (theta and phi), the planar nature of each detector and

[2]Compare to HST, for example, which can resolve to the hundredths of arcsecond level.

the LIGO-Virgo three detector network could break that symmetry.

The three model PSFs should be considered as possible predictions for typical accuracies. The low accuracy model may be typical for events detected with a three-detector LIGO/Virgo network at the threshold of detectability, and medium accuracies possible for higher SNRs. Meanwhile, the addition of a fourth interferometer, such as a possible AIGO detector in Australia or LGCT in Japan, could significantly enhance the sky localization accuracy and moderately improve distance sensitivity, making medium-accuracy measurements typical and high-accuracy measurements possible.

5.1 Bayesian Analysis

Bayes' equation (Eq. 5.1) is simply a pragmatic restatement of the commutative nature of logic (Eq. 5.2[3]; Bretthorst, 1988).

$$P(M_i|D_j) = \frac{P(D_j|M_i) \cdot P(M_i)}{P(D_j)} \tag{5.1}$$

$$P(M, D|I) = P(M|D, I) \cdot P(D|I) = P(D|M, I) \cdot P(M|I) = P(D, M|I) \tag{5.2}$$

Bayes' theorem is used to find the probability that a hypothesis/model M is true given data D $[P(M_i|D_j)]$, by using the probability of theoretical obtaining the data if the model were true $[P(D_j|M_i)]$. The 'prior probability for the model' [or *Bayesian Prior*–$P(M_i)$] incorporates any prior information for or against the model, while the 'prior probability for the data' [or *Evidence*–$P(D_j)$] acts as a normalization constant. Throughout our analysis, we are concerned with the ability to distinguish between models based on observations *per se*, and therefore use flat priors [i.e. $P(M_i) = P(M_j)$] and equivalent evidence [i.e. $P(D_i) = P(D_j)$]. Additionally, both terms cancel when we compare different models.

We use data sets $D_j \in \{D_{360}, D_{180}, D_{90}\}$ which are drawn from each model $M_i \in \{M_{360}, M_{180}, M_{90}\}$ respectively. Each data set is composed of n-independently drawn data

[3]Equation 5.2 includes the prior information 'I'–left out of equation 5.1 for clarity.

points (tracer positions), defined by a weight (linearly proportional to its progenitor-halo's mass m_h, as discussed in §3.1) and 3 position coordinates r, θ and ϕ (or right ascension and declination, equivalently): $D_i(n) = \{x_{i,1}(m_h, r, \theta, \phi)\ ...\ x_{i,n}(m_h, r, \theta, \phi)\}$. We can then write the probability that a particular model 'i' fits a data set 'j' as:

$$\frac{P(M_i|D_i(n))}{P(M_j|D_i(n))} = \frac{P(D_i(n)|M_i)}{P(D_i(n)|M_j)} = \prod_{k=1}^{n} \frac{P(x_{i,k}|M_i)}{P(x_{i,k}|M_j)} \tag{5.3}$$

To take into account the especially large positional uncertainties in reconstructing source locations, every data point is convolved with some point spread function 'S' describing the detector response, i.e.

$$P_{\rm pos}(x, \theta, \phi) = \int\int\int P_{\rm event}(x', \theta', \phi') \cdot S(x - x', \theta - \theta', \phi - \phi') dx' d\theta' d\phi' \tag{5.4}$$

In equation 5.4, $P_{\rm pos}$ is the probability of associating an event with a particular position, and $P_{\rm event}$ is the probability of the event occurring at a particular position. For a discrete sample-space of m pixels l, this can be rewritten as

$$P(x_{i,k}|M_j) = \sum_{l=1}^{m} S(x_{i,k}|{\rm pixel}_l) \cdot P({\rm pixel}_l|M_j) \tag{5.5}$$

For a given PSF, we now have the tools to compute the certainty with which we can ascribe some number of events to a certain model, the number of events required to reach a desired confidence level, or the required detector accuracy to reach that confidence.

5.2 Observational Requirements

From each model (M_{360}, M_{180}, and M_{90}) we create 50 'data sets' (D_{360}, D_{180}, and D_{90}), each composed of 1000 tracers. Using Eqs. 5.3 and 5.5, we find the number of data points ('detections') required to distinguish between models with 99% confidence, in 90% (45/50) of data sets. This is repeated for each PSF, and two sample volumes (40 and 80 Mpc). The number of detections required in each case are summarized in table 5.2.

		$M_{360}(D_{360})$		$M_{180}(D_{180})$		$M_{90}(D_{90})$	
Dist	PSF Accuracy	vs. M_{180}	vs. M_{90}	vs. M_{360}	vs. M_{90}	vs. M_{360}	vs. M_{180}
$\leq$ 80Mpc	High	22	16	26	>1000	22	282
	Med	73	39	35	>1000	31	384
	Low	>1000	349	52	>1000	50	881
$\leq$ 40Mpc	High	27	17	34	>1000	23	>1000
	Med	78	46	40	>1000	37	>1000
	Low	146	137	56	>1000	56	>1000

Table 5.2: Number of detections required to achieve 99% confidence in the correct model for 90% ($\frac{45}{50}$) of data sets, using three possible detector accuracies and two sample volumes. The three different detector accuracies are characterized by standard deviations in distance, right ascension and declination of: $\sigma_{high} = \{5\%, 1^\circ, 1^\circ\}$, $\sigma_{med} = \{30\%, 2^\circ, 2^\circ\}$, $\sigma_{low} = \{50\%, 4^\circ, 4^\circ\}$. Entries marked '$>1000$' never reached the desired confidence in the 1000 data points, for the required number of data sets.

We find that 50-100 events would be sufficient to distinguish between the lowest and highest kick-velocity scenarios for moderate (and plausible) detector accuracies. For low detector accuracies, 200-400 detections could be necessary. The easiest to distinguish case is that of the lowest kick-velocity (D_{90}), especially in comparison to the highest (vs. M_{360}). In our simulations, distinguishing between the two low-kick scenarios is very difficult, if not impossible. Both low-kicks are well below most halo escape velocities, and thus their distributions end up very similar (see Fig. 4.4). The only high-velocity contrast case which could not be distinguished was D_{360} vs. M_{180} at the lowest detector accuracies and the full sample volume. Overall, the results seem promising. For even the lowest detector accuracy, the highest and lowest velocity scenarios can be distinguished between with only hundreds of detections at most.

Readily apparent from table 5.2 is the asymmetry in distinguishing between model x and model y, with data drawn from model x; and that of distinguishing between model x and y, with data from model y. The data points from one model contain fundamentally different information than that of another. For instance, While only 50 detections are required to distinguish D_{90} from

M_{360}, almost 350 are required for D_{360} vs. M_{90}. While the detection of a handful of events clearly outside any host-galaxy would be hallmark of a strong kick–a sufficiently high signal to noise ratio for such a clear distinction is unlikely.

To investigate whether distance or angular resolution was limiting, we have explored numerous mixed PSF accuracies, described in table 5.3. The results are presented in table 5.4. Variation of other parameters were also explored, e.g. lowering the desired confidence to 90% and decreasing the number of required data sets (to 80%, 96%, and 98%), each with negligible effect on the resulting detection numbers.

	Standard Deviation in		
PSF Accuracy	Distance	Theta (deg)	Phi (deg)
High	5%	1°	1°
Ang Med	5%	2°	2°
Ang Low	5%	4°	4°
Dist Med	10%	1°	1°
Dist Low	20%	1°	1°

Table 5.3: Point-spread function parameters. Sampled data points are convolved with a PSF composed of a gaussian distribution with the given standard deviations in distance, theta, and phi.

Table 5.4 shows little difference between the highest accuracy PSF, and mixed accuracy ones; additionally, no additional trends are apparent as uncertainties increase. This suggests that neither angular nor radial uncertainty is independently limiting in deciphering the underlying source distribution. None-the-less, the sample will need to be significantly expanded–with many more data sets, and both a broader range and higher resolution of accuracy models–to fully ascertain the relative contribution to uncertainty from each degree of freedom. The benefits of adding a southern-hemisphere based gravitational wave interferometer to the system is an active area of interest (e.g. Barriga et al., 2010), and these factors should be better explored and taken into consideration.

	$M_{360}(D_{360})$		$M_{180}(D_{180})$		$M_{90}(D_{90})$	
PSF Accuracy	vs. M_{180}	vs. M_{90}	vs. M_{360}	vs. M_{90}	vs. M_{360}	vs. M_{180}
High	27	17	34	> 1000	23	> 1000
Ang Mid	31	19	31	384	24	320
Ang Low	41	23	43	486	24	318
Dist Mid	25	18	27	> 1000	22	172
Dist Low	44	21	27	> 1000	24	208

Table 5.4: Number of detections required to achieve 99% confidence in the correct model for 90% ($\frac{45}{50}$) of data sets, using mixed detector accuracy models. Data was only sampled from 40 Mpc. The different detector accuracies are detailed in table 5.1. Entries marked '> 1000' never reached the desired confidence in the 1000 data points for the required number of data sets.

6 Discussion

In this paper, we use dark matter cosmological simulations to examine the full three-dimensional distribution of coalescing compact binaries in the local universe under the following assumptions. First, we assume a single epoch of star formation and a simple star formation recipe; that is, the contribution of a particular halo to the total star formation is directly proportional to its dark matter mass. Although, more realistic treatment of star formation should be considered, we do not expect that our qualitative results will change significantly. Second, we assume an isotropic natal kick velocity distribution, whose properties are invariant of initial binary separation. Under this assumption, the merging time is independent of the kick velocity. This is found to be a reasonable approximation in binary population synthesis models, which helps justify our single epoch of tracer injection. Third, our comparisons between kick velocity models in §5 assume a perfect knowledge of the local dark matter distribution, when in actuality this distribution would have to be deduced from the observable, local universe. Finally, due to computational constraints, only an 80 Mpc region of the expected 400 Mpc horizon of advanced LIGO/Virgo has been modeled. Despite the increased uncertainty in the true-distance offset between host and merger at such distances, the difference between our 40 and 80 Mpc results (Table 5.2) suggest that our methods could remain effective in deducing the kick velocity distribution with a reasonable number of detections. Keeping these assumptions in mind, it is still evident that the use of static, non-evolving potentials for individual hosts at the time of binary formation severely overestimates the retention of all but the lowest barycentric velocity systems (Fryer et al., 1999; Belczyński et al., 2000; Rosswog et al., 2003; Bloom

et al., 1999; Bulik et al., 1999; Portegies Zwart & Yungelson, 1998).

Static calculations predict that the distribution of gravitational wave sources in the sky should closely trace the distribution of galaxies. An accurate inclusion of evolving host halo potentials in cosmological simulations have shown this to be inaccurate (Zemp et al., 2009). In fact, we show that not only do the distributions of merging compact binaries extend well beyond their birth halo, but variations in kick velocity lead to marked differences in their sky distributions. The repercussions of this result are twofold. On one hand, we find that the variation in the projected distribution of double compact objects with different natal kick-velocities should be distinguishable with the expected accuracies of GW observatories. In principle, this will allow important information on the formation and evolution of the binary progenitor to be deciphered from the distribution of GW detections alone. On the other hand, the fact that the distribution of merging binaries does not accurately trace the locations of their birth halos complicates redshift determination. Having said this, the presence of a binary distribution extending well beyond the half-light radius of their hosts suggests that associating optical counterparts to GW events could be easier as they are less likely to be drowned out by their host galaxy's light. This is particularly important as the optical counterparts are predicted to be relatively dim (Li & Paczyński, 1998; Rosswog & Ramirez-Ruiz, 2002; Kulkarni, 2005; Metzger et al., 2010).

Gravitational waves offer the possibility of casting proverbial light on otherwise invisible phenomena; they will–by their very nature–tell us about events where large quantitites of mass move in such small regions that they are utterly opaque and forever hidden from direct electromagnetic probing (see, e.g. Lee & Ramirez-Ruiz, 2007). A time-integrated luminosity of the order of a fraction of a solar rest mass is predicted from merging compact binaries. Ground-based facilities, like LIGO, GEO600 and Virgo, will be searching for these stellar mergers in the local universe. The distribution of merger sites is thus of considerable importance to GW observatories. Using cosmological simulations of structure formation, the local sky distributions are found to vary with the kick velocity distributions of the progenitor systems, allowing a determination of the cosmography

of massive binary stars. Despite the fact that individual detections lack the positional accuracy of electromagnetic observations, it may be possible to strengthen the case for (or against) high natal kick velocities based solely on GW observations.

Bibliography

Abadie, J., et al. 2010, ArXiv e-prints

Abbott, B. P., et al. 2009, Reports on Progress in Physics, 72, 076901

Acernese, F., et al. 2006, Classical and Quantum Gravity, 23, 635

Andersson, N. 2003, Classical and Quantum Gravity, 20, 105

Arras, P., & Lai, D. 1999, Phys. Rev. D, 60, 043001

Arzoumanian, Z., Chernoff, D. F., & Cordes, J. M. 2002, ApJ, 568, 289

Banerjee, S., Baumgardt, H., & Kroupa, P. 2010, MNRAS, 402, 371

Barriga, P., et al. 2010, Classical and Quantum Gravity, 27, 084005

Belczynski, K., Benacquista, M., & Bulik, T. 2008, ArXiv e-prints

Belczyński, K., Bulik, T., & Zbijewski, W. 2000, A&A, 355, 479

Belczynski, K., Kalogera, V., & Bulik, T. 2002, ApJ, 572, 407

Belczynski, K., Taam, R. E., Kalogera, V., Rasio, F. A., & Bulik, T. 2007, ApJ, 662, 504

Bloom, J. S., Sigurdsson, S., & Pols, O. R. 1999, MNRAS, 305, 763

Bondi, H., & Hoyle, F. 1944, MNRAS, 104, 273

Bretthorst, G. L. 1988, Bayesian Spectrum Analysis and Parameter Estimation (Springer-Verlag)

Brown, G. E. 1995, ApJ, 440, 270

Bulik, T., Belczyński, K., & Zbijewski, W. 1999, MNRAS, 309, 629

Camilo, F., Ng, C., Gaensler, B. M., Ransom, S. M., Chatterjee, S., Reynolds, J., & Sarkissian, J. 2009, ApJ, 703, L55

Campanelli, M., Lousto, C., Zlochower, Y., & Merritt, D. 2007, ApJ, 659, L5

Cavalier, F., et al. 2006, Phys. Rev. D, 74, 082004

Champion, D. J., Lorimer, D. R., McLaughlin, M. A., Cordes, J. M., Arzoumanian, Z., Weisberg, J. M., & Taylor, J. H. 2004, MNRAS, 350, L61

Chatterjee, S., & Cordes, J. M. 2004, ApJ, 600, L51

Chevalier, R. A. 1993, ApJ, 411, L33

—. 1996, ApJ, 459, 322

Cordes, J. M., Romani, R. W., & Lundgren, S. C. 1993, Nature, 362, 133

Counselman, III, C. C. 1973, ApJ, 180, 307

Cutler, C., & Flanagan, É. E. 1994, Phys. Rev. D, 49, 2658

Cutler, C., & Lindblom, L. 1996, Phys. Rev. D, 54, 1287

Damour, T., & Vilenkin, A. 2001, Phys. Rev. D, 64, 064008

Davies, M. B., Benz, W., & Hills, J. G. 1992, ApJ, 401, 246

Davis, M., Efstathiou, G., Frenk, C. S., & White, S. D. M. 1985, ApJ, 292, 371

Dimopoulos, S., Graham, P. W., Hogan, J. M., Kasevich, M. A., & Rajendran, S. 2009, Physics Letters B, 678, 37

Duquennoy, A., & Mayor, M. 1991, A&A, 248, 485

Dutton, A. A., van den Bosch, F. C., & Dekel, A. 2010, MNRAS, 608

Fairhurst, S. 2009, New Journal of Physics, 11, 123006

Fairhurst, S., & Mandel, I. 2011, In Preparation

Faulkner, A. J., et al. 2005, ApJ, 618, L119

Finn, L. S., & Chernoff, D. F. 1993, Phys. Rev. D, 47, 2198

Fixler, J. B., Foster, G. T., McGuirk, J. M., & Kasevich, M. A. 2007, Science, 315, 74

Fryer, C., Burrows, A., & Benz, W. 1998, ApJ, 496, 333

Fryer, C., & Kalogera, V. 1997, ApJ, 489, 244

Fryer, C. L., Holz, D. E., & Hughes, S. A. 2004, ApJ, 609, 288

Fryer, C. L., Woosley, S. E., & Hartmann, D. H. 1999, ApJ, 526, 152

Fukuda, Y., et al. 1998, Physical Review Letters, 81, 1562

Gauthier, D. J., Narum, P., & Boyd, R. W. 1986, Optics Letters, 11, 623

Gottardi, L. 2007, Phys. Rev. D, 75, 022002

Grojean, C., & Servant, G. 2007, Phys. Rev. D, 75, 043507

Guetta, D., & Piran, T. 2005, A&A, 435, 421

Hansen, B. M. S., & Phinney, E. S. 1997, MNRAS, 291, 569

Hartle, J. B. 2003, Gravity : an introduction to Einstein's general relativity, ed. Hartle, J. B.

Heger, A., Fryer, C. L., Woosley, S. E., Langer, N., & Hartmann, D. H. 2003, ApJ, 591, 288

High-Resolution Fly's Eye Collaboration et al. 2007, Astroparticle Physics, 27, 512

Hobbs, G., Lorimer, D. R., Lyne, A. G., & Kramer, M. 2005, MNRAS, 360, 974

Hoffman, Y., Martinez-Vaquero, L. A., Yepes, G., & Gottlöber, S. 2008, MNRAS, 386, 390

Horowitz, C. J. 2010, Phys. Rev. D, 81, 103001

Hughes, S. A. 2009, ARA&A, 47, 107

Hulse, R. A., & Taylor, H. J. 1974, in Bulletin of the American Astronomical Society, Vol. 6, Bulletin of the American Astronomical Society, 453–+

Hulse, R. A., & Taylor, J. H. 1975, ApJ, 195, L51

Iben, Jr., I., & Livio, M. 1993, PASP, 105, 1373

Jacoby, B. A., Cameron, P. B., Jenet, F. A., Anderson, S. B., Murty, R. N., & Kulkarni, S. R. 2006, ApJ, 644, L113

Jarosik, N., et al. 2011, ApJS, 192, 14

Kalogera, V. 1999, ApJ, 521, 723

Kalogera, V., Belczynski, K., Kim, C., O'Shaughnessy, R., & Willems, B. 2007, Phys. Rep., 442, 75

Kalogera, V., et al. 2004, ApJ, 601, L179

Kargaltsev, O., & Pavlov, G. G. 2009, ApJ, 702, 433

Kim, C., Kalogera, V., Lorimer, D. R., Ihm, M., & Belczynski, K. 2005, in Astronomical Society of the Pacific Conference Series, Vol. 328, Binary Radio Pulsars, ed. F. A. Rasio & I. H. Stairs, 83–+

Krolak, A., & Schutz, B. F. 1987, General Relativity and Gravitation, 19, 1163

Kulkarni, S. R. 2005, ArXiv Astrophysics e-prints (arXiv:astro-ph/0510256)

Kusenko, A. 2005, International Journal of Modern Physics A, 20, 1148

Lada, C. J. 2006, ApJ, 640, L63

Lai, D. 2000, in Stellar Astrophysics, ed. K. S. Cheng, H. F. Chau, K. L. Chan, & K. C. Leung, 127–+

Landau, L. D., & Lifshitz, E. M. 1975, The classical theory of fields, ed. Landau, L. D. & Lifshitz, E. M.

Larson, D., et al. 2010, ArXiv e-prints

Lee, W. H., & Ramirez-Ruiz, E. 2007, New Journal of Physics, 9, 17

Lee, W. H., Ramirez-Ruiz, E., & van de Ven, G. 2010, ApJ, 720, 953

Li, L., & Paczyński, B. 1998, ApJ, 507, L59

Livio, M., & Soker, N. 1988, ApJ, 329, 764

Lorimer, D. R., et al. 2006, ApJ, 640, 428

Lück, H., et al. 2006, Classical and Quantum Gravity, 23, 71

Lyne, A. G., Anderson, B., & Salter, M. J. 1982, MNRAS, 201, 503

Lyne, A. G., et al. 2000, MNRAS, 312, 698

Madau, P., Ferguson, H. C., Dickinson, M. E., Giavalisco, M., Steidel, C. C., & Fruchter, A. 1996, MNRAS, 283, 1388

Mandel, I. 2010, Private Communication

McLaughlin, M. 2003, in Chandra Proposal, 1614–+

Metzger, B. D., et al. 2010, MNRAS, 406, 2650

Meyer, F., & Meyer-Hofmeister, E. 1979, A&A, 78, 167

Michelson, A. A. 1924, ApJ, 60, 256

Moss, G. E., Miller, L. R., & Forward, R. L. 1971, Appl. Opt., 10, 2495

Moster, B. P., Somerville, R. S., Maulbetsch, C., van den Bosch, F. C., Macciò, A. V., Naab, T., & Oser, L. 2010, ApJ, 710, 903

Narayan, R., Piran, T., & Shemi, A. 1991, ApJ, 379, L17

Nice, D. J., Sayer, R. W., & Taylor, J. H. 1996, ApJ, 466, L87+

Ölmez, S., Mandic, V., & Siemens, X. 2010, Phys. Rev. D, 81, 104028

Oppenheimer, J. R., & Volkoff, G. M. 1939, Physical Review, 55, 374

O'Shaughnessy, R., Kim, C., Kalogera, V., & Belczynski, K. 2008, ApJ, 672, 479

Ostriker, J. P. 1975, in IAU Symposium, Vol. 73, Structure and Evolution of Close Binary Systems, ed. P. Eggleton, S. Mitton, & J. Whelan

Ott, C. D., Burrows, A., Livne, E., & Walder, R. 2004, ApJ, 600, 834

Paczynski, B. 1976, in IAU Symposium, Vol. 73, Structure and Evolution of Close Binary Systems, ed. P. Eggleton, S. Mitton, & J. Whelan, 75–+

Peters, P. C. 1964, Physical Review, 136, 1224

Peters, P. C., & Mathews, J. 1963, Physical Review, 131, 435

Phinney, E. S. 1991, ApJ, 380, L17

Podsiadlowski, P., Rees, M. J., & Ruderman, M. 1995, MNRAS, 273, 755

Portegies Zwart, S. F., & Yungelson, L. R. 1998, A&A, 332, 173

Postnov, K. A., & Yungelson, L. R. 2006, Living Reviews in Relativity, 9, 6

Prodi, G. A., et al. 2000, International Journal of Modern Physics D, 9, 237

Ramirez-Ruiz, E., & Lee, W. 2009, Nature, 460, 1091

Rosswog, S., & Ramirez-Ruiz, E. 2002, MNRAS, 336, L7

Rosswog, S., Ramirez-Ruiz, E., & Davies, M. B. 2003, MNRAS, 345, 1077

Sadowski, A., Belczynski, K., Bulik, T., Ivanova, N., Rasio, F. A., & O'Shaughnessy, R. 2008, ApJ, 676, 1162

Sandquist, E. L., Taam, R. E., & Burkert, A. 2000, ApJ, 533, 984

Schutz, B. F. 1986, Nature, 323, 310

Shimasaku, K., Hayashi, M., Motohara, K., Kashikawa, N., Kodama, T., & Ouchi, M. 2008, in Astronomical Society of the Pacific Conference Series, Vol. 399, Astronomical Society of the Pacific Conference Series, ed. T. Kodama, T. Yamada, & K. Aoki, 75–+

Smith, M. C., et al. 2007, MNRAS, 379, 755

Smith, T. L., Kamionkowski, M., & Cooray, A. 2006, Phys. Rev. D, 73, 023504

Spergel, D. N., et al. 2007, ApJS, 170, 377

Stadel, J. G. 2001, PhD thesis, UNIVERSITY OF WASHINGTON

Taam, R. E., & Ricker, P. M. 2010, New Astronomy Reviews, 54, 65

Taam, R. E., & Sandquist, E. L. 2000, ARA&A, 38, 113

Takahashi, R., & the TAMA Collaboration. 2004, Classical and Quantum Gravity, 21, 403

Terman, J. L., Taam, R. E., & Hernquist, L. 1995, ApJ, 445, 367

Thorne, K. S., & Zytkow, A. N. 1975, ApJ, 199, L19

—. 1977, ApJ, 212, 832

Thorsett, S. E., Dewey, R. J., & Stairs, I. H. 2005, ApJ, 619, 1036

Tolman, R. C. 1939, Physical Review, 55, 364

Weber, J. 1960, Phys. Rev., 117, 306

Weber, J. 1968, Phys. Rev. Lett., 20, 1307

Weisberg, J. M., & Taylor, J. H. 2005, in Astronomical Society of the Pacific Conference Series, Vol. 328, Binary Radio Pulsars, ed. F. A. Rasio & I. H. Stairs, 25–+

Weiss, R. 1972, Quarterly Progress Report of RLE, MIT, 105, 54

Willems, B., Vecchio, A., & Kalogera, V. 2008, Physical Review Letters, 100, 041102

Wolszczan, A. 1991, Nature, 350, 688

Wolszczan, A., Kulkarni, S. R., Middleditch, J., Backer, D. C., Fruchter, A. S., & Dewey, R. J. 1989, Nature, 337, 531

Zel'Dovich, Y. B., Ivanova, L. N., & Nadezhin, D. K. 1972, Soviet Ast., 16, 209

Zemp, M., Ramirez-Ruiz, E., & Diemand, J. 2009, ApJ, 705, L186

Zhou, L., et al. 2011, Chinese Physics Letters, 28, 013701

Zorotovic, M., Schreiber, M. R., Gänsicke, B. T., & Nebot Gómez-Morán, A. 2010, A&A, 520, A86+

Appendix A

A.1 Common Parameters

Name	Symbol	Value/Conversion
Solar Radius	$R_\odot$	6.995×10^8 m
Solar Mass	$M_\odot$	1.989×10^{30} kg
Astronomical Unit	AU	1.496×10^{11} m
Parsec	pc	3.086×10^{16} m

A.2 Common Initialisms

Initials	Term
BH	Black Hole
CE	Common Envelope
DBH	Double Black Hole (binary)
DCO	Double Compact Object
DM	Dark Matter
DNS	Double Neutron Star (binary)
GRB	Gamma Ray Burst
GW	Gravitational Waves
GWO	Gravitational Wave Observatory
MS	Main Sequence
MW	Milky Way
NS	Neutron Star
NS-BH	Neutron Star - Black Hole (binary)
PSF	Pount-Spread Function
SN(e)	Supernova(e)

A.3 Orbits

Consider two point-masses M_1, and M_2 in an orbit with semi-major axis a, eccentricity e, and period P (also orbital frequency $\Omega = \frac{2\pi}{P}$). Given the total mass of the system $M = M_1 + M_2$, we can define the reduced mass as $\mu = \frac{M_1 M_2}{M}$. By Kepler's third law

$$\Omega^2 = \left(\frac{2\pi}{P}\right)^2 = \frac{GM}{a^3} \tag{A.1}$$

which is to say, the angular frequency of the orbit (Ω) can be directly related to a. The average relative velocity of the stars will be

$$V = \sqrt{\frac{GM}{a}} \tag{A.2}$$

We also have a total energy E, and orbital angular momentum J

$$E = -\frac{GM_1M_2}{2a} \tag{A.3}$$

$$J = \mu\sqrt{GMa(1-e^2)} \tag{A.4}$$

In the center of mass frame, the angular velocity is given by

$$\omega = r^{-2}\sqrt{GMa(1-e^2)} \tag{A.5}$$

If at some time, we say the stars M_1 and M_2 are located at $\vec{r}_1 = (r_1\cos\theta, r_1\sin\theta, 0)$ and $\vec{r}_2 = (-r_2\cos\theta, -r_2\sin\theta, 0)$ respectively, with the x axis defined as zero when $\theta = 0$ is at pericenter, we can define the instantaneous separation between stars ($r = |\vec{r}| = |\vec{r}_1 + \vec{r}_2|$) as a function of θ:

$$r = \frac{a(1-e^2)}{1 + ecos\theta} \tag{A.6}$$

A.4 Publication

The Astrophysical Journal Letters, 725:L91–L96, 2010 December 10 doi:10.1088/2041-8205/725/1/L91

THE DISTRIBUTION OF COALESCING COMPACT BINARIES IN THE LOCAL UNIVERSE: PROSPECTS FOR GRAVITATIONAL-WAVE OBSERVATIONS

Luke Zoltan Kelley[1], Enrico Ramirez-Ruiz[1], Marcel Zemp[2], Jürg Diemand[3], and Ilya Mandel[4,5]
[1] Department of Astronomy and Astrophysics, University of California, Santa Cruz, CA 95064, USA; lzkelley@ucsc.edu
[2] Department of Astronomy, University of Michigan, Ann Arbor, MI 48109, USA
[3] Institute for Theoretical Physics, University of Zurich, 8057 Zurich, Switzerland
[4] MIT Kavli Institute, Cambridge, MA 02139, USA
Received 2010 September 2; accepted 2010 October 31; published 2010 November 23

ABSTRACT

Merging compact binaries are the most viable and best-studied candidates for gravitational-wave (GW) detection by the fully operational network of ground-based observatories. In anticipation of the first detections, the expected distribution of GW sources in the local universe is of considerable interest. Here we investigate the full phase-space distribution of coalescing compact binaries at $z = 0$ using dark matter simulations of structure formation. The fact that these binary systems acquire large barycentric velocities at birth ("kicks") results in merger site distributions that are more diffusely distributed with respect to their putative hosts, with mergers occurring out to distances of a few Mpc from the host halo. Redshift estimates based solely on the nearest galaxy in projection can, as a result, be inaccurate. On the other hand, large offsets from the host galaxy could aid the detection of faint optical counterparts and should be considered when designing strategies for follow-up observations. The degree of isotropy in the projected sky distributions of GW sources is found to be augmented with increasing kick velocity and to be severely enhanced if progenitor systems possess large kicks as inferred from the known population of pulsars and double compact binaries. Even in the absence of observed electromagnetic counterparts, the differences in sky distributions of binaries produced by disparate kick-velocity models could be discerned by GW observatories, within the expected accuracies and detection rates of advanced LIGO—in particular with the addition of more interferometers.

Key words: binaries: general – gravitational waves – stars: neutron

Online-only material: color figures

1. INTRODUCTION

The merger of double compact objects represents the first identified and most predictable source of gravitational-wave (GW) radiation (e.g., Phinney 1991). Only recently have the first GW observatories come online, and the first detection events are expected in the next few years. Over the past three decades the merger rate within the local universe has been thoroughly examined (see, e.g., Abadie et al. 2010; Mandel & O'Shaughnessy 2010 for recent reviews).

The merger rates are expected to be dominated by mergers of neutron-star binaries, with $\langle \Re \rangle \sim 1\,\mathrm{Mpc}^{-3}\,\mathrm{Myr}^{-1}$. However, these rates are significantly uncertain, since they come either from extrapolations from the small observed sample of Galactic binary pulsars whose luminosity distribution is not well constrained or from population-synthesis models that have many ill-determined parameters such as common-envelope efficiencies. In particular, Abadie et al. (2010) estimate the confidence bounds on the neutron-star binary merger rates as $\Re \approx 0.01$–$10\,\mathrm{Mpc}^{-3}\,\mathrm{Myr}^{-1}$. The horizon distances[6] for the initial and advanced LIGO/Virgo detector networks are estimated as $\mathcal{D} \sim 30$ and ∼400 Mpc, respectively, based on the distance at which a single detector could detect GWs from a neutron-star binary at a signal-to-noise ratio of 8. Abadie et al. (2010) estimate that the advanced LIGO/Virgo network could plausibly detect between 0.4 and 400 neutron-star binaries per year, with a likely rate of approximately 40 detections per year.

The prospects for detection and characterization of GW sources are thus sensitive to the distribution of compact binaries in the local universe. The fact that these systems must have large systemic velocities at birth (Brandt & Podsiadlowski 1995; Fryer & Kalogera 1997) implies that by the time they merge, after approximately a Hubble time, they will be far from their birth sites. The locations of merging sites depend critically on the binary's natal kick velocity and the temporal evolution of the gravitational potential of the host halo and its nearby neighbors (Zemp et al. 2009).

In this Letter, we study the evolving distribution of compact binary systems from formation until coalescence at $z = 0$ using cosmological simulations of structure formation. This allows us to examine the full radial and angular distributions of merging compact binaries in the local universe. In Section 2, we describe the numerical methods, initial setup, and the criteria used to select a local-like universe. The distributions of compact binaries at $z = 0$ are presented in Section 3 for three different kick-velocity scenarios, and in Section 4 we examine the ability of GW observatories to discern between them experimentally. Finally, Section 5 discusses the implications of our findings.

2. METHODS AND INITIAL MODEL

2.1. Simulation

The focus of this work is to understand the distribution of compact binaries in the local universe using cosmological simulations. To this end, we have performed a dark matter (DM) only cosmological structure formation simulation following the

[5] NSF Astronomy and Astrophysics Postdoctoral Fellow.
[6] The horizon distance is the maximum distance at which a signal can be detected with a given signal-to-noise threshold (e.g., 8); for a single detector, this is the distance at which gravitational waves from a face-on, overhead binary can be detected.

numerical procedure outlined in Zemp et al. (2009). A comoving 80 Mpc periodic box is initialized at redshift $z = 22.4$ (161 Myr) and uses WMAP3 cosmological parameters (Spergel et al. 2007). The initial conditions are evolved using the parallel tree code PKDGRAV2 (Stadel 2001) until $z = 1.60$ (4.24 Gyr). At this time, we populate each halo with mass greater than $2.15 \times 10^{11}\ M_{\odot}$ (of which there are 2461 in the simulation) with 2000 massless tracers.

Each tracer particle is meant to represent a compact binary system, which, on average, forms around the peak of the star formation epoch (Madau et al. 1996, 1998). In general, the local merger rate is given by the convolution of the star formation rate with the probability distribution of the merging time delays. Compact binaries formed at the peak of the star formation history, merging after delays consistent with the orbital separations of known relativistic binary pulsars (O'Shaughnessy et al. 2008), dominate the local merger rate.[7]

Tracers are injected into the center of their halo, with an isotropic Maxwell-Boltzmann velocity distribution with mean speeds $\bar{v} = 360$, 180, and 90 km s^{-1} and dispersions $\sigma = 150$, 75, and 37.5 km s^{-1} (hereafter denoted as models M_{360}, M_{180}, and M_{90}). This is consistent with the magnitude of the natal kicks required to explain the observed parameters of binary neutron star systems (Brandt & Podsiadlowski 1995; Fryer & Kalogera 1997)—only when the center of mass kicks have magnitudes exceeding 200 km s^{-1} can the progenitor orbits be sufficiently wide to accommodate evolved helium stars and still produce the small separations measured in these systems.

The contribution of individual tracers to the overall population is weighted linearly with their progenitor halo's mass (at $z = 1.6$) in all of our calculations.

Finally, the cosmological box together with the tracer particle populations are evolved until redshift $z = 0$ (13.8 Gyr). This results in diverse predictions of compact binary demographics at $z = 0$ in the case of an isotropic kick-velocity distribution whose properties are invariant to initial binary separation. Merger times in population-synthesis models are found to be relatively insensitive to the initial kick velocity (e.g., Bloom et al. 1999). This not only justifies our assumption but, when taken together with the progenitors' long time delays (O'Shaughnessy et al. 2010), also reinforces the validity of a single injection time.

2.2. Local-like Universe Selection

Once the tracers and DM are evolved to $z = 0$, a local-like universe is selected based on the following criteria (adapted from Hoffman et al. 2008).

1. There are two DM halos, representing the Milky Way and Andromeda pair, with maximum circular velocities $V_c \in [125, 270]$ km s^{-1}.
2. These halos are separated by $d \leqslant 1.4\ h^{-1}$ Mpc, and approaching each-other (i.e., $d \leqslant 0.0$ km s^{-1}).
3. There is a Virgo-like halo at a distance $d \in [5, 12]\ h^{-1}$ Mpc, with $V_c \in [500, 1500]$ km s^{-1}.
4. No halos with comparable or higher maximum circular velocities than either of the pair exist within $3\ h^{-1}$ Mpc, and no other Virgo-like halos exist within $12\ h^{-1}$ Mpc.

The first three constraints resulted in three local-like groups. Inclusion of the fourth criterion resulted in a single, optimal environment for our analysis.

[7] For $P(\tau) \propto 1/\tau$ this early-assembled population could increase the local event rate by at least ~3 (Guetta & Piran 2005).

3. THE LOCAL DISTRIBUTION OF COMPACT BINARIES

We now examine the local, three-dimensional distribution of merging compact binaries—characterized here by the massless tracer particle population at $z = 0$ centered on the Milky Way like galaxy. Figure 1 shows the radial distribution of tracers and DM within our local-like universe. In models M_{180} and M_{90}, tracer particles closely follow the DM central-density peaks, just like the galaxies themselves in cold dark matter (CDM) cosmology (Blumenthal et al. 1984).

As the kick velocity becomes comparable to the escape velocity of the progenitor halos, an increasing fraction of tracers escape. These unbound tracers form an intergalactic background which closely follows the overall DM distribution, as seen for model M_{360} in Figure 1. In super-galactic regions with more continuous gravitational potentials, the tracer background becomes more heavily populated. The relative isolation of the Milky Way–Andromeda pair contributes to the enduring presence of strong native tracer peaks located at each halo center. As a result, the extended background distributions of tracers—centered on the pair—are only apparent in the highest kick-velocity model.

As seen in Figure 2, the number of tracers within a sphere encompassing the Milky Way and Andromeda halos is noticeably depleted at higher kick velocities. At these velocities, the host halos are unable to effectively retain most of their tracers. As the sphere's volume approaches the Virgo cluster, the number of (sub)halos becomes so large that the mean separation between central peak densities decreases below the characteristic size of the background tracer population. As a result, the variation with kick velocity in the tracer distributions is drowned-out. It should be noted that the expected event rate in such a small volume is negligible (Abadie et al. 2010); thus the effects of varying kick velocity will be indiscernible in the integrated merger-rate of compact objects within LIGO/Virgo detection horizons.

Although the integrated tracer distribution is insensitive to the model, the angular distribution of tracers depends strongly on the binary's kick velocity. This is evident in Figure 3, which plots sky maps of tracers and DM within a given volume. As expected, high velocity kicks lead to more pronounced isotropies when compared to the low kick scenarios. At 10 Mpc, ~40% of the M_{360} weighted tracers lie in pixels outside those of M_{90}; this fraction falls to 15% and 10% for 40 and 80 Mpc, respectively. This trend results from the increasing isotropy of DM in projection at progressively larger scales.

For large velocities, the distribution of GW sources forms a sky continuum (Figure 3) rather than well-isolated substructures—complicating host galaxy identification and thus redshift determination. On the other hand, with large kick velocities the majority of mergers will take place well outside the host galaxy's half-light radius, aiding the detection of photonic counterparts—especially at optical wavelengths.

4. PREDICTIONS FOR GRAVITATION WAVE OBSERVATIONS

The number of detections required for GW observatories to be able to reconstruct the kick-velocity distribution is examined here. Timing triangulation from relative GW phase shifts[8] between widely separated detectors is the primary source of sky localization (Fairhurst 2009), and Fisher matrix or Markov Chain Monte Carlo techniques can be used to compute

[8] For a review of GW emission from compact binaries see Hughes (2009).

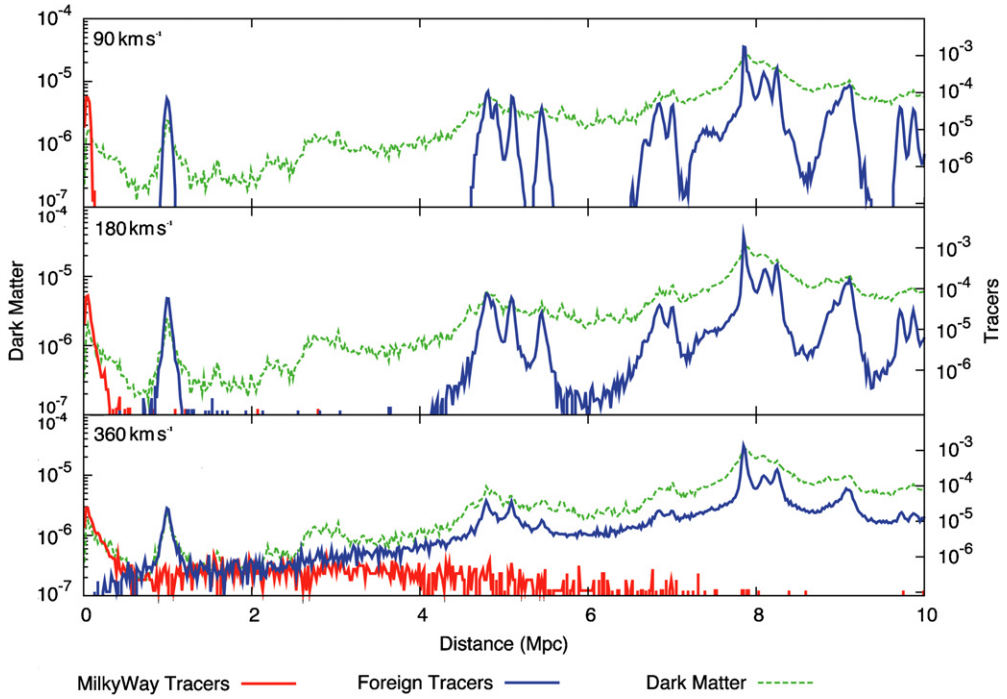

Figure 1. Tracer vs. dark matter distribution in a local-like universe as a function of barycentric kick velocity. Integrated particle mass in uniform radial-width shells is plotted vs. distance from a solar-equivalent offset from the Milky Way center. The vertical axes are plotted in arbitrary units of number per unit length, with tracers normalized with respect to the total population as described in Section 2.1. As the kick velocity increases from 90 km s^{-1} (top panel) to 360 km s^{-1} (bottom panel), a noticeable portion of tracers becomes delocalized.

(A color version of this figure is available in the online journal.)

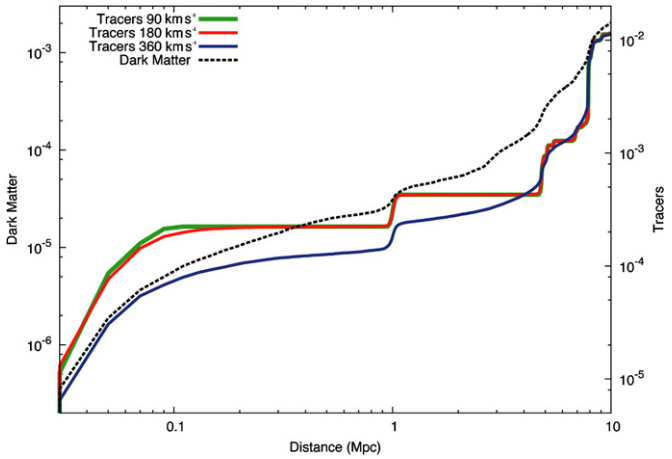

Figure 2. Cumulative distribution of tracers and dark matter as a function of kick velocity. The vertical axes are plotted in arbitrary units of number per unit volume, with tracers normalized. Although the number of tracers in the central halo is noticeably lower for the highest kick-velocity model, the difference is negligible once the volume reaches the Virgo-like cluster.

(A color version of this figure is available in the online journal.)

error estimates (van der Sluys et al. 2008). The intricacies of parameter determination and error estimation can be extensive, as correlations between waveform parameters mean that some parameters (such as distance and inclination) are partially degenerate (see, e.g., Cutler & Flanagan 1994, and references therein). Typically, with a three-detector network, the distance to the GW event could be determined to within a ∼20%–50% uncertainty, and the angular location of the event to ∼5–50 square degrees, depending on source location, masses, and signal-to-noise ratio (Fairhurst 2009; van der Sluys et al. 2008). The large uncertainty in the distance determination can be understood when considering its dependence on the signal amplitude, which is much more uncertain than the phase-space information.

To estimate the number of events required to distinguish between different kick-velocity models, we apply a Bayesian approach similar to that used by Mandel (2010) to approximate the efficacy of population reconstruction from GW signals. Data sets $D_j \in D_{360}, D_{180},$ and D_{90} are drawn from each model $M_i \in M_{360}, M_{180},$ and M_{90}, respectively. Each data set contains n independently drawn data points (i.e., tracers), characterized by three position coordinates; i.e., $D_i(n) = [x_{i,1}(r, \alpha, \delta), x_{i,2}(r, \alpha, \delta), \ldots x_{i,n}(r, \alpha, \delta)]$. The probability of a tracer being selected for a given data set is linearly proportional to the halo mass of the progenitor (see Section 2.1). The probability that a particular model i fits a data set j can be rewritten using Bayes' formula:

$$P(M_i|D_j(n)) = \frac{P(D_j(n)|M_i) \cdot P(M_i)}{P(D_j(n))}. \quad (1)$$

Throughout our analysis we assume flat priors $[P(M_i) = P(M_j)]$, and equivalent evidence $[P(D_i) = P(D_j)]$. A comparison between models then yields

$$\frac{P(M_i|D_i(n))}{P(M_j|D_i(n))} = \frac{P(D_i(n)|M_i)}{P(D_i(n)|M_j)} = \prod_{k=1}^{n} \frac{P(x_{i,k}|M_i)}{P(x_{i,k}|M_j)}, \quad (2)$$

where the probability of a particular data point given a specific model, $P(x_{i,k}|M_j)$, is described by the convolution of the point-spread function (PSF–S) of the detector with the probability

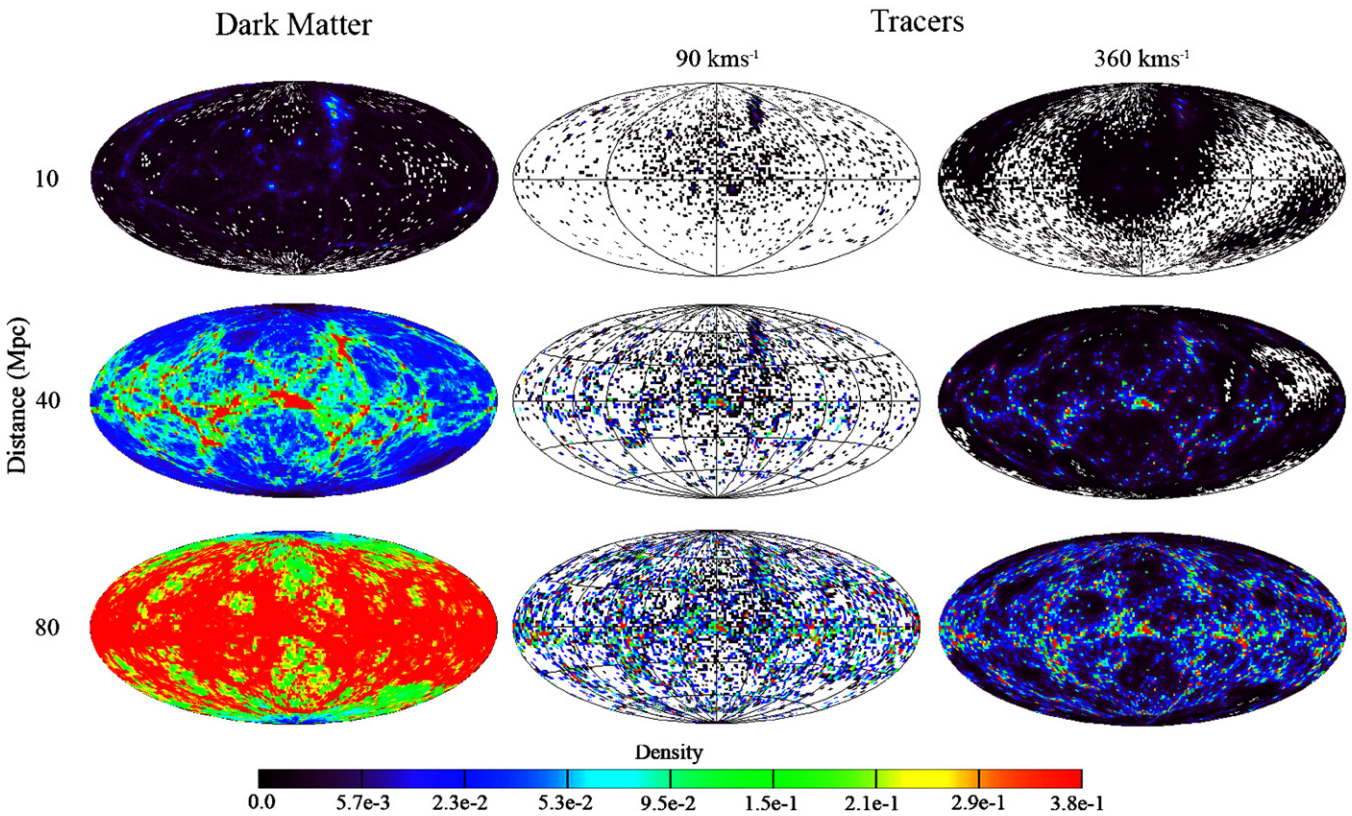

Figure 3. Sky maps of dark matter and tracers with highest and lowest kick-velocity scenarios as a function of distance. Dark matter and normalized-tracer column densities are scaled independently and logarithmically (in $2^\circ \times 2^\circ$ bins), with white pixels corresponding to densities less than the resolution of the simulation. Although tracer peak densities remain relatively unchanged, a strong tracer-background forms as the kick velocity approaches the escape velocity. Differences in tracer distributions are clearly apparent.

(A color version of this figure is available in the online journal.)

Table 1
Number of Detections Required to Achieve 99% Confidence in the Correct Model for 90% ($\frac{45}{50}$) of Data Sets

Dist	PSF Accuracy	$M_{360}(D_{360})$		$M_{180}(D_{180})$		$M_{90}(D_{90})$	
		vs. M_{180}	vs. M_{90}	vs. M_{360}	vs. M_{90}	vs. M_{360}	vs. M_{180}
	High	22	16	26	>1000	22	282
⩽80 Mpc	Med	73	39	35	>1000	31	384
	Low	>1000	349	52	>1000	50	881
	High	27	17	34	>1000	23	>1000
⩽40 Mpc	Med	78	46	40	>1000	37	>1000
	Low	146	137	56	>1000	56	>1000

Notes. These results are compared between two different sample radii, and three different detector accuracies characterized by standard deviations (in distance, right ascension, declination) of: $\sigma_{\rm high} = \{5\%, 1^\circ, 1^\circ\}$, $\sigma_{\rm med} = \{30\%, 2^\circ, 2^\circ\}$, $\sigma_{\rm low} = \{50\%, 4^\circ, 4^\circ\}$. Entries marked ">1000" failed to reach the desired confidence in the required number of data sets within the 1000 data points used.

distribution function of the model in question. That is

$$P(x_{i,k}|M_j) = \sum_{l=1}^{q} S(x_{i,k}|\text{pixel}_l) \cdot P(\text{pixel}_l|M_j), \qquad (3)$$

where the sum is being performed on each pixel (pixel_l) for all q pixels.

The PSFs are assumed here to be Gaussian in each coordinate direction, characterized by standard deviations in distance, right ascension, and declination: $\sigma_{\rm high} = [5\%, 1^\circ, 1^\circ]$, $\sigma_{\rm med} = [30\%, 2^\circ, 2^\circ]$, $\sigma_{\rm low} = [50\%, 4^\circ, 4^\circ]$. These reflect different assumptions for the high, medium, and low accuracy of positional reconstruction for GW detections. The exact parameter-estimation accuracy is difficult to predict, since it will depend both on the details of the detector network (e.g., the relative sensitivity of detectors and their calibration accuracy) and on the specifics of individual events (their signal-to-noise ratio, and the sky location and binary orientation). Therefore, these three assumptions should be considered only as possible predictions for typical accuracies. Thus, low accuracies may be typical for events detected with a three-detector LIGO/Virgo network at the threshold of detectability. Meanwhile, the addition of a fourth interferometer, such as a possible AIGO detector in Australia or LGCT in Japan, could significantly enhance the sky localization accuracy and moderately improve distance sensitivity (S. Fairhurst et al. 2011, in preparation), making medium-accuracy measurements typical and high-accuracy measurements possible.

In these calculations, we compare hypothetical GW observations with models of compact binary distributions. This comparison is being made assuming that the local DM distribution is perfectly known. In reality, this is not the case; and the results presented here are thus optimistic. In the future, the comparison between model and observation should be refined to include the local distribution of light (e.g., galaxies) rather than DM halos.

Table 1 summarizes the ability of GW observatories to discern the kick-velocity distribution of the merging binaries from the reconstructed angular positions and distances (assumed to be determined without a galaxy host association). Sample volumes of 40 and 80 Mpc are considered in order to understand the sensitivity of our results to the uncertainty in physical separation which, for a fixed angular resolution, varies with distance. We find that ∼50 events are required to distinguish between the lowest and highest kick-velocity scenarios for moderate detector accuracies, irrespective of sample volume. For low detector accuracies, 50–350 detections are necessary.[9] Thus, a distinction between the two extreme models is possible once advanced detectors come online, with an expected event rate of ∼40 per year for detections of binary neutron-star mergers (Abadie et al. 2010).[10] Meanwhile, distinguishing between the two low-kick scenarios is very difficult, if not impossible, until the era of third-generation detectors. The addition of a fourth GW detector to the LIGO/Virgo network would significantly improve source localization, and thereby the accuracy with which event distributions could be distinguished.

Assuming a LIGO/Virgo horizon of ∼400 Mpc, only ∼10% of all detected mergers would take place within 80 Mpc. With a constant angular resolution, the uncertainty in physical position is proportional to the event's distance, suggesting that using events at greater distances leads to a degradation in the ability to distinguish between kick-velocity models. Although we find no clear increase in the number of required detections between the 40 and 80 Mpc samples, further investigation is required to assess the effects of a larger sample volume.

5. SUMMARY

In this Letter, we use DM cosmological simulations to examine the full three-dimensional distribution of coalescing compact binaries in the local universe under the following assumptions. First, we assume a single epoch of star formation proportional to the progenitor DM halo's mass. Although a more realistic treatment of star formation should be considered, we do not expect that our qualitative results will change significantly. Second, we assume an isotropic natal kick-velocity distribution, whose properties are invariant of initial binary separation. This is found to be a reasonable approximation in binary population-synthesis models, which helps justify our single epoch of tracer injection. Third, our comparisons between kick-velocity models in Section 4 assume a perfect knowledge of the local DM distribution. Finally, due to computational constraints, only an 80 Mpc region of the expected 400 Mpc horizon of advanced LIGO/Virgo has been modeled. Despite the increased uncertainty in the true-distance offset between host and merger at such distances, the difference between our 40 and 80 Mpc results (Table 1) suggests that our methods could remain effective. Keeping these assumptions in mind, it is still evident that the use of static, non-evolving potentials for individual hosts at the time of binary formation severely overestimates the retention of all but the lowest barycentric velocity systems (Fryer et al. 1999; Belczyński et al. 2000; Rosswog et al. 2003; Bloom et al. 1999; Bulik et al. 1999; Portegies Zwart & Yungelson 1998).

In contrast to static calculations, we show that not only do the distributions of merging compact binaries extend well beyond their birth halo, but variations in kick velocity lead to marked differences in their sky distributions. As a result, we find that double compact objects with different natal kick velocities should be distinguishable with the expected accuracies of GW observatories. In principle, this will allow important information on the formation and evolution of the binary progenitor to be deciphered from the distribution of GW detections alone. On the other hand, the fact that the distribution of merging binaries does not accurately trace the locations of their birth halos complicates redshift determination. Having said this, the presence of a binary distribution extending well beyond the half-light radius of their hosts suggests that associating optical counterparts to GW events could be easier as they are less likely to be drowned out by their host galaxy's light. This is particularly important as the optical counterparts are predicted to be relatively dim (Li & Paczyński 1998; Rosswog & Ramirez-Ruiz 2002; Kulkarni 2005; Metzger et al. 2010).

GWs offer the possibility of casting proverbial light on otherwise invisible phenomena; they will—by their very nature—tell us about events where large quantities of mass move in such small regions that they are utterly opaque and forever hidden from direct electromagnetic probing (see, e.g., Lee & Ramirez-Ruiz 2007). Ground-based facilities, such as LIGO, GEO600, and Virgo, will be searching for these stellar-remnant mergers in the local universe. The distribution of merger sites is thus of considerable importance to GW observatories. The proposed use of galaxy catalogs as priors when passing triggers from possible GW detections to point telescopes for electromagnetic follow-ups will need to account for the possibility of mergers away from observed galaxies. Despite the fact that individual GW detections lack the positional accuracy of electromagnetic observations, determination of the cosmography of massive binary stars is still possible based solely on GW observations. The addition of more GW detectors to the LIGO/Virgo network will greatly improve our ability to distinguish between models with different kick-velocity distributions by improving the positional reconstruction of individual events.

We thank C. Fryer, V. Kalogera, and R. O'Shaughnessy for useful discussions and the referee for constructive comments. We acknowledge support from NASA NNX08AN88G and NNX10AI20G (L.Z.K. and E.R.), the David and Lucile Packard Foundation (E.R.); NSF grants: AST-0847563 (L.Z.K. and E.R.), AST-0708087 (M.Z.), AST-0901985 (I.M.); and the Swiss National Science Foundation (J.D.). Computations were performed on the Pleaides UCSC computer cluster.

[9] It is important to note that the number of detections required is highly sensitive to the model from which the data is drawn, not simply on which models are being contrasted.

[10] The event rate estimates have significant uncertainties, and range from pessimistic estimates of ∼0.4 events per year to optimistic estimates of ∼400 events per year (Abadie et al. 2010).

REFERENCES

Abadie, J., et al. 2010, Class. Quantum Grav., 27, 173001
Belczyński, K., Bulik, T., & Zbijewski, W. 2000, A&A, 355, 479
Bloom, J. S., Sigurdsson, S., & Pols, O. R. 1999, MNRAS, 305, 763
Blumenthal, G. R., Faber, S. M., Primack, J. R., & Rees, M. J. 1984, Nature, 311, 517
Brandt, N., & Podsiadlowski, P. 1995, MNRAS, 274, 461

Bulik, T., Belczyński, K., & Zbijewski, W. 1999, MNRAS, 309, 629
Cutler, C., & Flanagan, É. E. 1994, Phys. Rev. D, 49, 2658
Fairhurst, S. 2009, New J. Phys., 11, 123006
Fryer, C., & Kalogera, V. 1997, ApJ, 489, 244
Fryer, C. L., Woosley, S. E., & Hartmann, D. H. 1999, ApJ, 526, 152
Guetta, D., & Piran, T. 2005, A&A, 435, 421
Hoffman, Y., Martinez-Vaquero, L. A., Yepes, G., & Gottlöber, S. 2008, MNRAS, 386, 390
Hughes, S. A. 2009, ARA&A, 47, 107
Kulkarni, S. R. 2005, arXiv:astro-ph/0510256
Lee, W. H., & Ramirez-Ruiz, E. 2007, New J. Phys., 9, 17
Li, L., & Paczyński, B. 1998, ApJ, 507, L59
Madau, P., Ferguson, H. C., Dickinson, M. E., Giavalisco, M., Steidel, C. C., & Fruchter, A. 1996, MNRAS, 283, 1388
Madau, P., Pozzetti, L., & Dickinson, M. 1998, ApJ, 498, 106
Mandel, I. 2010, Phys. Rev. D, 81, 084029
Mandel, I., & O'Shaughnessy, R. 2010, Class. Quantum Grav., 27, 114007
Metzger, B. D., et al. 2010, MNRAS, 406, 2650
O'Shaughnessy, R., Kalogera, V., & Belczynski, K. 2010, ApJ, 716, 615
O'Shaughnessy, R., Kim, C., Kalogera, V., & Belczynski, K. 2008, ApJ, 672, 479
Phinney, E. S. 1991, ApJ, 380, L17
Portegies Zwart, S. F., & Yungelson, L. R. 1998, A&A, 332, 173
Rosswog, S., & Ramirez-Ruiz, E. 2002, MNRAS, 336, L7
Rosswog, S., Ramirez-Ruiz, E., & Davies, M. B. 2003, MNRAS, 345, 1077
Spergel, D. N., et al. 2007, ApJS, 170, 377
Stadel, J. G. 2001, PhD thesis, Univ. Washington
van der Sluys, M. V., et al. 2008, ApJ, 688, L61
Zemp, M., Ramirez-Ruiz, E., & Diemand, J. 2009, ApJ, 705, L186